



**HAL**  
open science

## First 18650-format Na-ion cells aging investigation: A degradation mechanism study

Long H. B. Nguyen, Paula Sanz Camacho, Jérémie Fondard, Dany Carlier, Laurence Croguennec, Maria Rosa Palacín, Alexandre Ponrouch, Cecile Courreges, Rémi Dedryvère, Khiem Trad, et al.

### ► To cite this version:

Long H. B. Nguyen, Paula Sanz Camacho, Jérémie Fondard, Dany Carlier, Laurence Croguennec, et al.. First 18650-format Na-ion cells aging investigation: A degradation mechanism study. *Journal of Power Sources*, 2022, 529, pp.231253. 10.1016/j.jpowsour.2022.231253. hal-03607692

**HAL Id: hal-03607692**

**<https://univ-pau.hal.science/hal-03607692v1>**

Submitted on 17 Mar 2022

**HAL** is a multi-disciplinary open access archive for the deposit and dissemination of scientific research documents, whether they are published or not. The documents may come from teaching and research institutions in France or abroad, or from public or private research centers.

L'archive ouverte pluridisciplinaire **HAL**, est destinée au dépôt et à la diffusion de documents scientifiques de niveau recherche, publiés ou non, émanant des établissements d'enseignement et de recherche français ou étrangers, des laboratoires publics ou privés.

# First 18650-Format Na-ion Cells Aging Investigation: A Degradation Mechanism Study

*L.H.B. Nguyen<sup>1,2,8,\*</sup>, P. Sanz Camacho<sup>1</sup>, J. Fondard<sup>4</sup>, D. Carlier<sup>1,8,9</sup>, L. Croguennec<sup>1,8,9</sup>, M.R. Palacin<sup>3,9</sup>, A. Ponrouch<sup>3,9</sup>, C. Courrèges<sup>4,8,9</sup>, R. Dedryvère<sup>4,8,9</sup>, K. Trad<sup>5</sup>, C. Jordy<sup>6</sup>, S. Genies<sup>7</sup>, Y. Reynier<sup>7</sup>, L. Simonin<sup>7,\*</sup>.*

<sup>1</sup> Univ. Bordeaux, CNRS, Bordeaux INP, ICMCB, UMR CNRS 5026, F-33600, Pessac, France.

<sup>2</sup> Laboratoire de Réactivité et Chimie des Solides, UMR CNRS 7314, Université de Picardie Jules Verne, F-80039 Amiens Cedex 1, France.

<sup>3</sup> Institut de Ciència de Materials de Barcelona (ICMAB-CSIC) Campus UAB, E-08193 Bellaterra, Catalonia, (Spain).

<sup>4</sup> IPREM, CNRS, Univ. Pau & Pays Adour, E2S UPPA, 64000 Pau, France.

<sup>5</sup> VITO/EnergyVille, Unit Energy Technology, Thor Park 8310, 3600 Genk, Belgium

<sup>6</sup> SAFT, 111 Boulevard Alfred Daney, F-33074 Bordeaux, France

<sup>7</sup> CEA-LITEN, Univ. Grenoble Alpes, 17 rue des Martyrs, F-38054, Grenoble Cedex 9, France.

<sup>8</sup> RS2E, Réseau Français sur le Stockage Electrochimique de l'Energie, FR CNRS 3459, F-80039 Amiens Cedex 1, France.

<sup>9</sup> ALISTORE-ERI European Research Institute FR CNRS 3104, Amiens, F-80039 Cedex 1, France.

\*Corresponding Authors: Long H.B. Nguyen ([longuyen@ucsd.edu](mailto:longuyen@ucsd.edu)) and Loïc Simonin ([Loic.Simonin@cea.fr](mailto:Loic.Simonin@cea.fr))

## Abstract

Several Hard carbon||Na<sub>3</sub>V<sub>2</sub>(PO<sub>4</sub>)<sub>2</sub>F<sub>3</sub> full-cells in 18650-format are assembled to demonstrate the possible use of SIBs in stationary applications. The cell aging process is investigated in two different conditions: (i) continuous cycling at different current rates, and (ii) storage at different states-of-charge at various temperatures. The obtained results reveal that the cell degradation depends strongly on the temperature, current rates applied in cycling conditions, or state-of-charge of the storage test. Under cycling conditions, the continuous sodiation/desodiation may induce significant mechanical deformation, leading to the detachment of active materials from the current collector. Furthermore, the post-mortem analysis shows that reaction rate and aging process are not homogeneous along the electrode roll. The XRD analysis shows that Na<sub>3</sub>V<sub>2</sub>(PO<sub>4</sub>)<sub>2</sub>F<sub>3</sub> structure is robust; nevertheless, the material cannot recover the initial Na<sup>+</sup> content as the cycling progresses, which is the main cause for capacity loss in the positive electrode. The solid-electrolyte interphase present on the hard carbon surface was characterised using XPS. The hard carbon electrode cannot be detected during this study, evidencing the formation of a relatively thick (> 5 nm) passivating layer composed of carbonate salts and NaF, which are the main products of electrolyte decomposition.

## 1. Introduction

Degradation of battery performance upon lifetime is common to all battery technologies [1] and is typically rooted in parasitic reactions, which may involve both active (electrode materials, electrolyte) and inactive (current collectors, separator) battery components. The type of such reactions and the extent to which they occur depends not only on the battery chemistry but also on the battery design and, most importantly, on operation conditions (temperature, cycling rate, state of charge during storage).

Research on this complex topic, especially for the Li-ion technology, has been intensified in the last years due to the entering of this technology into transportation and grid applications for which the enhancement of cycle life is compulsory. In portable electronic devices, the need for Li-ion batteries (LIBs) to outlive the devices they power has been much easier to fulfill. It is now generally accepted that the aging in Li-ion cells is related to either loss of lithium inventory related to consumption of lithium ions by parasitic reactions (film formation, electrolyte decomposition, lithium plating) or loss of active material in the electrodes either due to particle cracking, delamination or partial dissolution [2–6]. While the loss of performance at the negative electrode is rooted in Solid Electrolyte Interphase (SEI) instability (enhanced at higher temperatures) and lithium metal plating (intensified at low temperatures) [7], on the positive electrode, it is caused mainly by the partial dissolution of the active material during cycling/storage or electrolyte oxidation, which is promoted by temperature and high potential.

In parallel to efforts aiming at understanding the fundamentals lying behind the battery aging process, the scientific community has recently and intensively dedicated significant efforts to the development of new alternative battery chemistries, which would ultimately not involve the use of lithium, which is a relatively scarce element in the earth crust. Amongst these, the sodium-ion battery (SIB) concept is especially attractive. Indeed, sodium is widely abundant, and it has chemical analogies with lithium, which could result in accelerated technology development by taking advantage of the comprehensive accumulated know-how in LIBs [8–11]. Nevertheless, some relevant differences between both technologies should be considered when developing this new battery chemistry. For example, the conventional negative electrode for LIBs, graphite, does not insert sodium unless it is solvated to form ternary intercalation compounds [12], and up to now, only hard carbon (HC) exhibits realistic application prospects [13–15]. The feasibility of SIBs using hard carbon negative electrodes is beyond any doubt [11,16], and many start-up companies are currently manufacturing prototype cells involving different positive electrode materials [17–19]. Amongst these concepts, the one using polyanion

$\text{Na}_3\text{V}_2(\text{PO}_4)_2\text{F}_3$  (denoted NVPF hereafter) as positive electrodes stands out for its high average voltage and high rate capabilities [20–24].

It is well reported in the literature that LIBs are sensitive to temperature, current rates, storage state-of-charge (SoC), cycling potential window, and of course, time [25–35]. Similar to LIBs, Na-ion batteries are also expected to have performance fade over time and use. Some published papers have discussed in detail the performance degradation in half-cells using sodium counter electrodes [36–38]; aging studies on full-cells, to the best of our knowledge, have never been reported before. For this purpose, test protocols were selected to investigate the impact of these aging factors on the sodium-ion cells used in this study. The post-mortem analysis on the aged cells may identify predominant mechanisms taking place and thus help design age-resistant battery materials.

In this study, several Hard carbon|| $\text{Na}_3\text{V}_2(\text{PO}_4)_2\text{F}_3$  full-cells in 18650-format were assembled to demonstrate the feasibility of using SIBs in stationary applications. The assembled cells showed little electrochemical performance variability thanks to an optimised fabrication process, ensuring that conclusions drawn from one cell represent the whole series. They were subjected to aging tests in (i) continuous cycling at different current rates, simulating the cell degradation in actual working conditions, and (ii) storage at different states-of-charge and various temperatures. The capacity degradation was followed through several quick check-ups. At the end of the test, the cells were disassembled for autopsy, and the two electrodes, negative and positive, were recovered for post-mortem analyses with X-ray diffraction, solid-state nuclear magnetic resonance, and X-ray photoelectron spectroscopies. Combining bulk and surface-sensitive techniques helped us obtain insightful information on the degradation process taking place in the bulk of the active materials and the passivating layer.

## 2. Experimental

### 2.1. Cell manufacturing and initial formation process

The NVPF active material was prepared following a previously reported process at the scale of 1 kg per batch [39]. The hard carbon electrode material was Carbotron P(J) purchased from Kureha. The casted electrodes were prepared following a standard procedure using a high-speed disperser to process the ~ 17 kg slurry batch (7.1 kg NVPF and 6.5 kg HC) and a pilot slot die COATEMA<sup>®</sup> coater (3 m long oven). For NVPF, a 190 m long electrode was cast on a 20  $\mu\text{m}$  thick Al current collector with a 110 mm width and a mass loading of 12  $\text{mg}\cdot\text{cm}^{-2}$  where 91

wt.% of it is NVPF. For HC, a 100 m long electrode was produced on a 20  $\mu\text{m}$  Al current collector. Its width was 180 mm, and its mass loading was 6  $\text{mg}\cdot\text{cm}^{-2}$ . The HC/NVPF capacity ratio in the first cycle is 1.12 while the reversible HC/NVPF capacity in later cycles is 1.03.

36 cells in 18650-format were then made. This format, first introduced by Sony in 1991, is a standard for Li-ion cells, often used to benchmark materials. The cylindrical 18 mm diameter and 65 mm high cell uses a steel casing and a crimped tight cap, including safety features. The electrodes (~50 cm long) are wound together with a separator (Celgard polyolefin) to form the so-called “jelly rolls”. 1M  $\text{NaPF}_6$  in ethylene carbonate and dimethyl carbonate (EC/DMC = 1/1) with 1.5 wt.% of fluoroethylene carbonate (FEC) additive was used as electrolyte. The electrolyte was prepared in an Ar fill glove box (moisture < 2 ppm) by mixing  $\text{NaPF}_6$  (from Stella Chemifa Corp., moisture < 50 ppm) with an EC/DMC 1/1 volume mixture (from UBE Corp., moisture < 10 ppm) and 1.5w% of FEC (fluoroethylene carbonate, from SOLVAY). The average weight of the cells was 32.5 g. The cells’ formation was carried out between 4.25 V and 2 V with a first cycle at C/10 current rate, followed by a C/5 capacity check. The nominal capacity used for formation was 750 mAh. Rate capability was measured at 25°C and 45°C and from C/3 to 5C discharge rate with constant C/3 charge rate between each, in the same voltage window.

## 2.2. Aging Tests

The aging tests consisted of cycle-life and calendar tests (also known as storage tests). In these conditions, the charge C-rate, the temperature, and the state-of-charge of the cell during storage were varied to investigate their effects on the cell’s lifetime. These different aging conditions are summarised in **Table S1** and **Table S2**. Every test was performed on two different cells to confirm the repeatability of the results.

The cycle-life tests consisted of constant current charge-discharge cycles within a fixed voltage window varying from 2.0 V to 4.25 V, corresponding to 100%  $\Delta\text{SoC}$ . They were performed at two different temperatures: 25°C and 45°C, and at charge/discharge C-rates of C/5, 1C, and 2C. The aging tests were interrupted to conduct check-up tests to measure changes in the performances of the cells. Note that these check-up tests should ideally not have any impact on cell degradation. Two protocols were used: the extended and the short check-up tests. The first one was performed before starting and at the end of the aging test (State of Health (SoH) = 80% and/or a specific duration/number of cycles). The extended check-up test consisted of a capacity

test at different discharge C-rates (C/20, C/5, C/3, C/2, 1C, 2C, and 5C) and a charge and discharge pulse test (30 s at 1C). The short check-up test was performed at shorter and regular intervals (every 28 days), consisting of two standard cycles with a C/5 current rate and a charge and discharge pulse test.

The calendar aging tests were performed by storing the cells at different SoC (30%, 50%, and 100%), at a constant temperature (5°C, 25°C, or 45°C), and open-circuit voltage (OCV) value. The calendar test conditions and the number of cells used in this experiment are summarised in **Table S2**. Regular check-up tests were performed to determine the remaining capacity during the aging process, and the calendar test terminated when the cell's SoH = 80%.

**2.3. Cell dismantling and sample preparation.** Before dismantling, the cells were discharged at a C/10 current rate until the minimum voltage of 2.0 V was reached. This voltage was maintained until the current was less than or equal to C/100. This two-step discharge protocol with constant current and voltage ensuring that all electrochemically active sodium ions were stored in the positive electrode, leaving the negative electrode free of exchangeable sodium regardless of the cells' aging state. Indeed, aged cells could have highly polarised discharge curves, leading the cell to reach the end-of-discharge voltage quickly when Na<sup>+</sup> might not be wholly re-intercalated into the positive electrode. The discharged cells were disassembled in an Argon-filled glove box using cutting tools such as DREMEL<sup>TM</sup> or a ceramic cutter. A careful unrolling process was performed to avoid shortcuts between electrodes and prevent biased results.

Several Na<sub>x</sub>V<sub>2</sub>(PO<sub>4</sub>)<sub>2</sub>F<sub>3</sub> references were prepared to help interpret <sup>23</sup>Na and <sup>31</sup>P solid-state nuclear magnetic resonance spectra recorded on the cycled electrodes. These references were prepared in small quantity (~ 5 mg) by cycling Na||NVPF half-cells at C/20 current rate (per Na<sup>+</sup>). The amount of extracted Na<sup>+</sup> was controlled by limiting the charging time corresponding to the number of exchanged electrons. These Na<sub>x</sub>V<sub>2</sub>(PO<sub>4</sub>)<sub>2</sub>F<sub>3</sub> references were prepared in small quantity to make sure the homogeneity of the samples. The samples recovered after cycling were washed with dimethyl carbonate and dried under vacuum before being characterized by <sup>23</sup>Na, <sup>31</sup>P ss-NMR, and then XRD. To perform ss-NMR measurements, the samples were packed in a 2.5 mm rotor requiring ~ 10 mg of material for the rotor to be fully packed, the samples were thus mixed with KBr. That is why KBr diffraction peaks were observed in all reference samples.

## 2.4. Post-mortem characterization

For all characterization techniques, the samples were always stored or handled under argon atmosphere to avoid any contact with air or moisture.

**X-ray diffraction (XRD)** patterns of the post-mortem samples were recorded on a Philips PW3830 diffractometer, equipped with a Cu  $K_{\alpha 1,2}$  irradiation source, using a conventional air-tight sample holder. The data were recorded in the  $2\theta$  angular range of  $5^\circ$ – $120^\circ$ , with a step size of  $0.02^\circ$  and a counting time of 10 s per step. The profile matching was performed on the obtained data using the FullProf suite program [40].

**$^{23}\text{Na}$  solid-state nuclear magnetic resonance (ss-NMR)** spectra were acquired on a Bruker Avance III 500 MHz spectrometer, equipped with an 11.7 T wide-bore magnet (operating at the Larmor frequency of 132.3 MHz for  $^{23}\text{Na}$ ). Experiments were performed using a conventional 2.5 mm MAS probe with a 30 kHz MAS rate. Chemical shifts were referenced relative to an aqueous 1M NaCl solution at 0 ppm. A short pulse length of 1  $\mu\text{s}$  corresponding to a selective  $\pi/8$  pulse determined using a 1 M NaCl aqueous solution was employed in each case. The spectral width was set to 1 MHz and the recycle delay of 0.2 s, long enough to avoid  $T_1$  saturation effects. The baseline distortions resulting from the spectrometer dead time (8  $\mu\text{s}$ ) were removed computationally using a polynomial baseline correction routine. The obtained data were processed by TopSpin and DM-fit software [41].

**$^{31}\text{P}$  solid-state nuclear magnetic resonance** spectra were acquired on a Bruker Avance III 100 MHz spectrometer, equipped with a 2.4 T wide-bore magnet (operating at Larmor frequency of 40.6 MHz for  $^{31}\text{P}$ ), using a standard Bruker 2.5 mm MAS probe at 30 kHz MAS rate. Chemical shifts were referenced relative to an aqueous  $\text{H}_3\text{PO}_4$  85% (Sigma-Aldrich) solution at 0 ppm. A Hahn echo sequence was used with a  $\pi/2$  pulse of 1  $\mu\text{s}$ , and a recycle delay of 0.2 s.

**X-ray photoelectron spectroscopy (XPS)** data were collected with a Thermo Scientific Escalab 250 Xi spectrometer using focused monochromatised radiation at Al  $K_{\alpha}$   $h\nu = 1486.6$  eV photon energy. The analysed area of the samples was a  $450 \times 900 \mu\text{m}^2$  ellipse. Core peaks were recorded with a constant pass energy of 20 eV. The binding energy scale was calibrated from the hydrocarbon C 1s peak at 285.0 eV or the carbon Super P at 284.5 eV. The XPS introduction transfer chamber was directly connected to an argon glovebox, in which the samples were prepared. Before analysis, both negative and positive electrodes were washed three times by 1 min immersion in pure anhydrous DMC baths to get rid of the  $\text{NaPF}_6$  salt

precipitated on the electrodes' surface. DMC was then evaporated by leaving the electrodes under vacuum (using the glovebox antechamber) for at least 1 hour.

### 3. Results

#### 3.1. Initial tests

Thirty-six 18650-format cells were assembled in this study, and the initial electrochemical properties of these cells are gathered in **Table S3**. All the cells reached an average specific energy of 83 Wh·kg<sup>-1</sup> at C/10 with 20.6% of irreversible capacity in the first cycle of the formation. The average charge capacity in the first cycle referred to the amount of NVPF is 129 mAh·g<sup>-1</sup>, which is in good agreement with the values obtained for this material in half-cells [23,24,42,43]. Average normalised resistance was measured at 51 Ohm·cm<sup>-2</sup>. The dispersion in the observed values was low, owing to the pilot coatings used to manufacture the cells.

Rate capability was measured for the first batch of six cells at 25°C and 45°C and from C/3 to 5C discharge rates with a constant C/3 charge rate between each (**Figure 1**). Very stable rate capability was observed with only a small voltage drop at high current rates but without the sloping voltage curve, characteristic of diffusion limitations. Higher temperature resulted in a more significant capacity recovery, probably due to the enhanced electrolyte conductivity at 45°C (**Figure 1**). The same test results at 25°C on six representative cells are featured in **Figure S1**. More than 85% of energy retention and 92% of capacity retention were obtained at a 5C discharge rate.

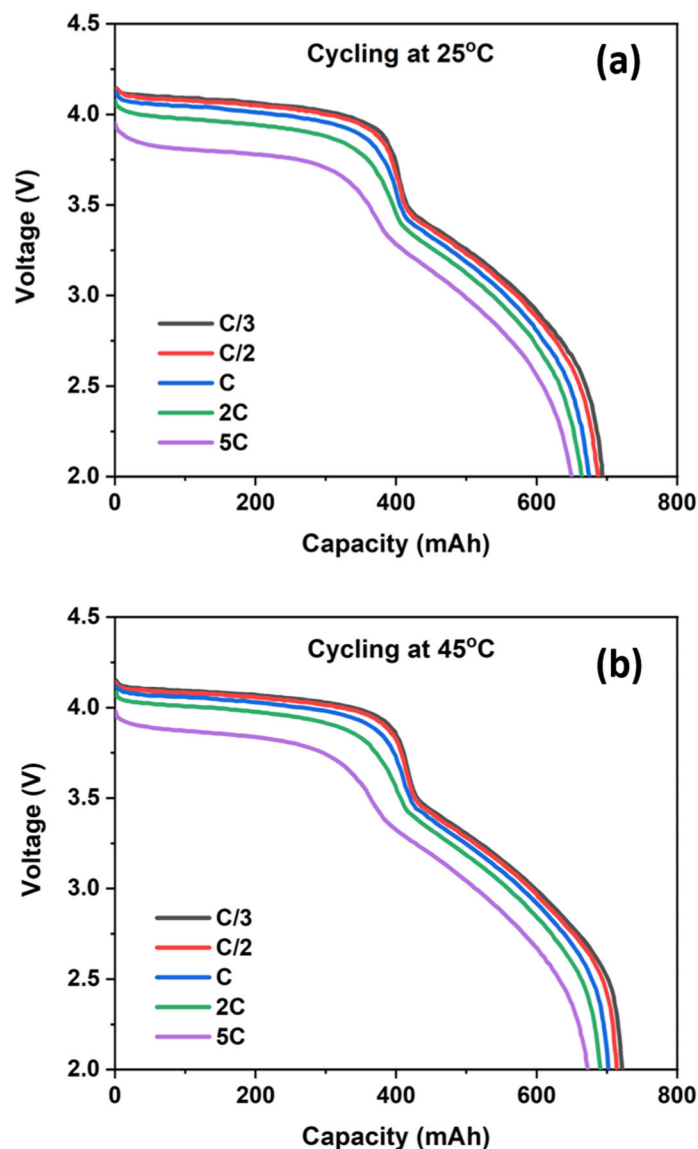


**Figure 1.** 18650-cells discharge rate capability at (a) 25°C and (b) 45°C.

Pulse discharge resistance (using a pulse length of 30 s at 2C current) was also measured as a function of SoC at 25°C and 45°C (**Figure S2**). The resistance increased gradually when SoC decreased, apart from a spike around 43% of total capacity. This feature was due to two potential steps of NVPF during discharge. Since there was 0.5 V difference between the two voltage plateaus of NVPF, the apparent resistance taken around 43% SoC appeared to be more significant. On the other hand, the stable high voltage of 4 V, coupled with low resistance in this region, allowing highpower applications. A significant temperature effect was observed with a decrease of ~30% in resistance when moving from 25°C to 45°C (**Figure S2**).

### 3.2. Cycling tests

As the life-cycling tests were performed using different current rates, it is convenient to use the total throughput capacity (Ah) and the number of equivalent cycles to compare different sets of results. The total throughput capacity represents the total discharge and charge capacities measured through the complete test. The equivalent cycle number is the results of dividing the total throughput capacity by the capacity of one complete cycle (including charge and discharge), which is 1.4 Ah ( $2 \times 0.7\text{Ah}$ ) in this study. As the check-up tests may contribute to the overall capacity loss, the capacity exchanged during check-up tests was also included.

The percentage of capacity loss was calculated based on the discharge capacity (C/5 constant current followed by constant voltage with a C/25 cut-off rate) measured at the second standard cycle.

$$\text{Capacity loss (\%)} = \frac{(C_0 - C_i)}{C_0} \times 100$$

with  $C_i$  being the discharge capacity measured at the end of the second standard cycle of the check-up test and  $C_0$  being the discharge capacity measured at the end of the second standard cycle of the first check-up test (initial capacity).

**Figure 2a** compares the capacity loss measured during check-ups of the cells cycled at 25°C and those at 45°C. It was clear that compared to the test conducted at 25°C, higher temperatures increased the capacity fading rate. **Figure 2b** also shows the evolution of the cells' discharge capacity loss, cycled at 25°C and different C-rates. The cells aged with C/5 and 2C current rates showed excellent reproducibility; however, the two cycled at 1C show a significant deviation (**Figure 2b**). The cells cycled at the highest C-rate (2C) degraded less than those cycling at lower C-rate (C/5). This behaviour is consistent with the electrolyte faster degradation at low C-rates, especially at high SoC levels (*i.e.*, high voltage). Interestingly, cycling at a low C-rate at 25°C induces faster cell degradation than at 1C and 45°C (**Figure S3**). Post-mortem analysis of the cells with XRD, ss-NMR, and XPS was performed in order to identify the nature and the quantity of the degradation products and detect changes in the active materials, if any.

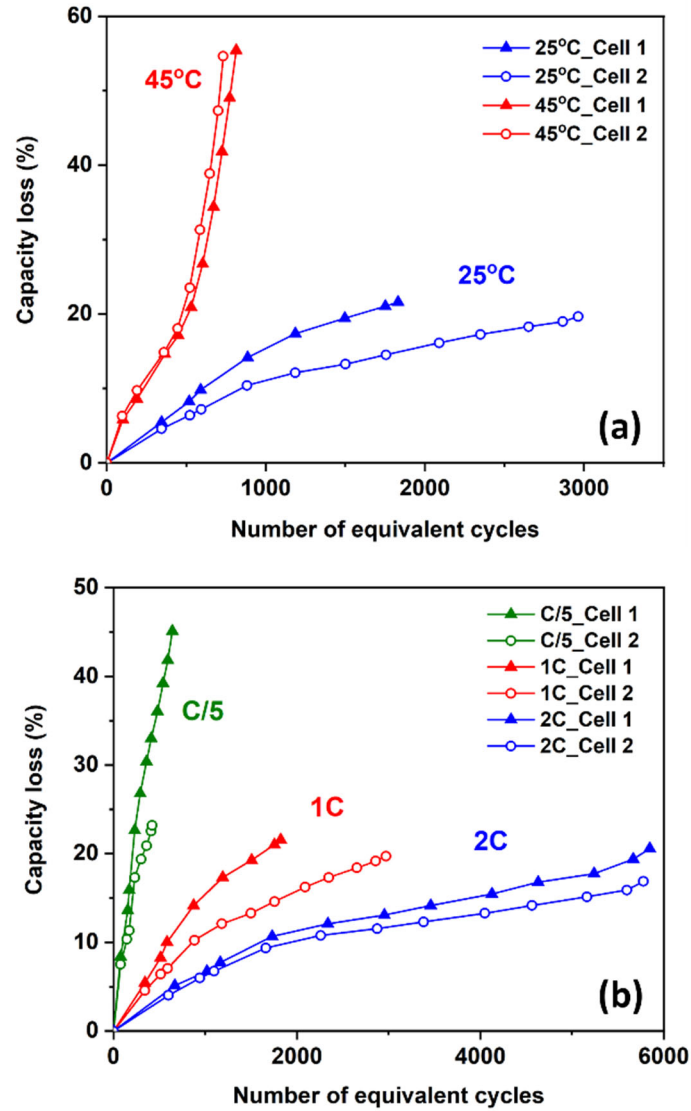


**Figure 2.** (a) Capacity loss for cells cycled at 1C at 25°C and those cycled at 1C at 45°C. (b) Capacity loss as a function of number of equivalent cycles for cells charged at different C-rates at 25°C.

### 3.3. Calendar tests

Two main factors that may influence the cell aging process during storage are SoC and temperature. In order to decorrelate the impact of these two factors, two sets of experiments were performed: (i) the cells' SoC were set at 100% and the degradation was followed at different temperatures, and (ii) the storage temperature was fixed at 25°C while the cells were stored at different SoCs.

**Impact of temperature on the aging process.** Several cells were stored at 100% SoC and different temperatures (5°C, 25°C, and 45°C) for up to one year. These tests were interrupted

regularly, and a check-up test was then performed to check their remaining capacity. The calendar test terminated when the cell's SoH reached 80%.

As can be inferred from the plots depicted in **Figure 3a**, the cells stored at 100%SoC and 45°C showed a higher degradation rate than those stored at 5°C and 25°C, which could be due to the lower stability of the electrolyte at elevated temperatures. Furthermore, the cell's internal resistance increased gradually during the storage time (**Figure 3b**), which was undoubtedly a consequence of the continuous electrolyte degradation when stored at 100% SoC. Discharge capacity at different C rates was evaluated for all the cells at the end of the storage test and compared to the values obtained initially (**Figure 3c**). The results clearly indicate that storage resulted in capacity loss, and the extent of which was more important at higher temperatures as the electrode/electrolyte degradation was more severe.

**Impact of state of charge.** Several cells were stored at 25°C and different SoCs (30%, 50%, and 100%) for more than one year. The impact of SoC on the capacity loss and the internal resistance after storage at 25°C is presented in **Figures S4a** and **S4b**, respectively. A higher capacity loss was observed at 100% SoC most likely due to electrolyte instability, caused by a direct contact with fully charged negative and positive electrode materials at potentials close to 0 and 4.25 V vs. Na<sup>+</sup>/Na, respectively. As expected, the cell's internal resistance increased faster when the storage test was performed at 100% of SoC.

The obtained results confirm that both temperature and SoC have significant impacts on the aging process. The best conditions for HC||NVPF cells to have a long-life duration upon storage are 25°C and 30% SoC. Since the capacity loss was more severe at 100% SoC and 45°C; hence, post-mortem analyses will be performed for cells stored under these conditions.

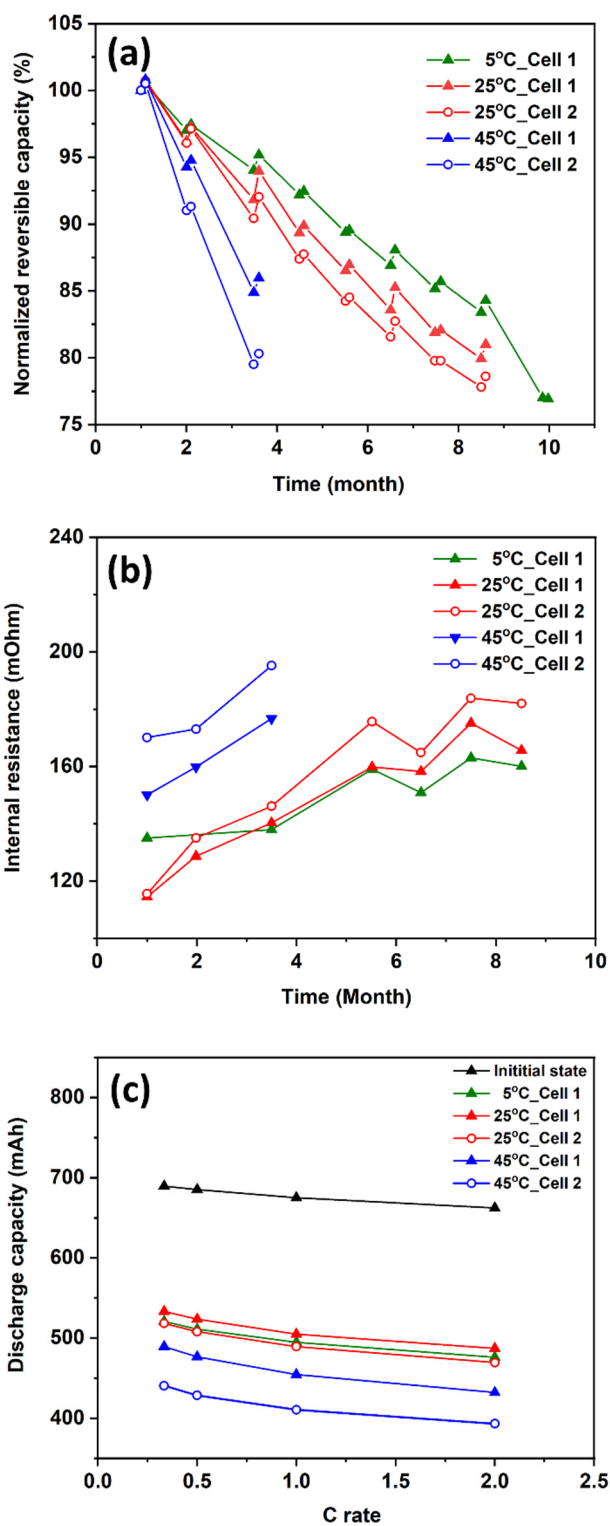


**Figure 3.** (a) Normalized reversible capacity of the cells stored at 100% SoC, at 5°C, 25°C, and 45°C. The discharge capacity was measured at a C/5 current rate and the calendar test terminated when the cell's SoH reached 80%. (b) Impact of temperature on the internal resistance measured at 50% of discharge after one month of storage at 100% SoC. (c) Discharge capacity measured at the end of the storage test at 100% SoC. The discharge capacity of a fresh cell is depicted as a reference.

### 3.4. Post-mortem characterization

Post-mortem tests were done on the materials recovered from two HC||NVPF full-cells to investigate the influence of the temperature and the cycling conditions on the cell's degradation process. The first cell was cycled continuously in the potential range of 2.0 – 4.25 V with a current rate of 1C at 45°C. The cell lost 43% of its initial capacity after 800 cycles before dismantling at discharged state. The second cell was stored at 100% SoC and 45°C for nearly four months, and it was discharged at a C/10 rate until the minimum voltage of 2.0 V before dismantling.

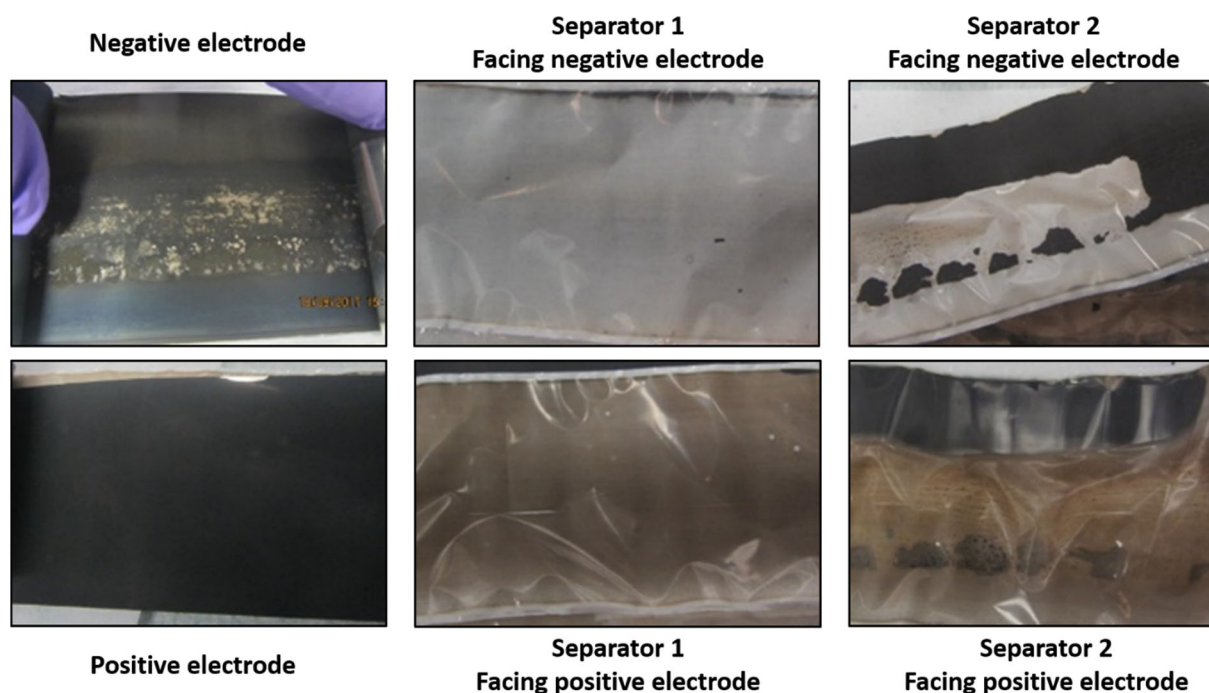


**Figure 4.** Images of the electrodes and the separators recovered from a HC// NVPF full-cell after 800 cycles in the potential range of 2.0 – 4.25 V with a current rate of 1C at 45°C.

**Visual inspection.** Images of the cells' electrodes and separators recovered after long-term cycling at 1C and 45°C are depicted in **Figure 4**. After cycling, the negative electrode presented bright deposits in the middle all along the electrode. Such deposits were not observed for the aged electrode in calendar conditions (**Figure S5**). Contrary to the stored electrode, this cycled electrode was folded in the core, likely a consequence of mechanical stress associated with the sodium insertion/de-insertion in the active material. Furthermore, when we were trying to remove the negative electrode roll from the separator, some parts of the electrode were detached from the current collector and remained adherent to the separator (**Figure 4**). The electrode

detachment was observable only on the side facing the case, *e.g.*, separator 2 (**Figure 4**). In contrast, the positive electrode seemed not to be damaged, except for some small and clearer halos visible on the stored positive electrode and in the separator facing it (**Figure S5**), attributed to tiny gas bubbles formed due to electrolyte decomposition. This feature was also observable on the separator facing the positive electrode of the cycled cell, becoming completely brown, except in some small spherical areas remaining white after the cycling. One can speculate that in these areas, the separator was not directly in contact with the positive electrode surface because of the gas bubbles, and thus it did not get colored. On the other hand, the separators showed no degradation after the calendar test (**Figure S5**).

**X-ray diffraction characterization.** The positive electrodes recovered after the aging tests (long-term cycling and calendar tests) were analyzed by powder X-ray diffraction (XRD) to detect the structural modifications that may occur in the material after applying different cycling conditions. The XRD patterns recorded on the positive electrode recovered after the long-term cycling test at 45°C, at the beginning, middle, and end of the roll, are depicted in **Figure 5a**. They show the presence of well-defined diffraction peaks, which testified the stability of the NVPF structural framework, even after 800 cycles. Nonetheless, the difference in the relative intensity of the diffraction peaks recorded at different parts of the recovered electrode implies an inhomogeneity in the Na-content along the electrode. Furthermore, none of them resembled the XRD pattern of the pristine material NVPF, indicating that the cycled electrode could not recover its initial Na-content after 800 cycles, despite the full discharge protocol applied before the dismantling of the cell.

Several  $\text{Na}_x\text{V}_2(\text{PO}_4)_2\text{F}_3$  samples with different values of  $x$  were prepared *ex situ*, and their XRD patterns were used as reference to estimate the Na-content in each part of the recovered electrode (**Figure S6**). Unfortunately, none of the XRD patterns resembled exactly any reference pattern. The asymmetry, the broadening, and the splitting of some diffraction peaks indicated the presence of at least two different  $\text{Na}_x\text{V}_2(\text{PO}_4)_2\text{F}_3$  compositions in each sample. Profile matching analysis was carried out and the  $\text{Na}_x\text{V}_2(\text{PO}_4)_2\text{F}_3$  compositions present in each part of the electrode were estimated from the calculated  $V/Z$  values (**Table 1**) and the standard line given in **Figure S7**. The profile matching analyses performed on the XRD patterns recorded for the beginning, middle, and end of the roll, recovered from the aging cycling test are given in **Figures S8-S11**. A mixture of  $\text{Na}_{2.2}\text{V}_2(\text{PO}_4)_2\text{F}_3$  and “ $\text{Na}_{2.3}\text{V}_2(\text{PO}_4)_2\text{F}_3$ ” was detected at the beginning of the recovered electrode, which might be a consequence of inhomogeneity in  $\text{Na}^+$

distribution between different particles. The middle of the recovered electrode was characterised by the co-existence of two different phases with the “ $\text{Na}_{2.3}\text{V}_2(\text{PO}_4)_2\text{F}_3$ ” composition (**Table 1**). Even though the nominal composition was the same, the  $\text{Na}^+$  distribution might not be identical, leading to the formation of a series of local domains that were close in composition and characterised by a slight mismatch in their corresponding cell parameters. At the end of the aged electrode, there was a surprising existence of two phases with a significant compositional difference, “ $\text{Na}_{2.7}\text{V}_2(\text{PO}_4)_2\text{F}_3$ ” and  $\text{Na}_{2.2}\text{V}_2(\text{PO}_4)_2\text{F}_3$  (**Table 1**), indicating inhomogeneity in  $\text{Na}^+$  content in different particles.

By *operando* synchrotron XRD, we have earlier reported that neither “ $\text{Na}_{2.3}\text{V}_2(\text{PO}_4)_2\text{F}_3$ ” nor “ $\text{Na}_{2.7}\text{V}_2(\text{PO}_4)_2\text{F}_3$ ” intermediate phases could be isolated [44]. The *operando* experiment reported in previous study had been performed on the first charge of a fresh  $\text{Na}||\text{NVPF}$  half-cell; however, in this study,  $\text{HC}||\text{NVPF}$  full-cells were used and XRD patterns were recorded at the end of discharge where the cells had been working for several cycles. The inability to recover the initial composition,  $\text{Na}_3\text{V}_2(\text{PO}_4)_2\text{F}_3$ , or a composition close to it is due to the fact that a significant amount of  $\text{Na}^+$  stock was lost in the first cycle as irreversible capacity related to the formation of the SEI layer on HC electrode. The loss of  $\text{Na}^+$  inventory is thus the cause of the observation of non-equilibrium compositions, “ $\text{Na}_{2.3}\text{V}_2(\text{PO}_4)_2\text{F}_3$ ” and “ $\text{Na}_{2.7}\text{V}_2(\text{PO}_4)_2\text{F}_3$ ”. Moreover, the inhomogeneity in the internal pressure at different zones of the jelly roll and the temperature gradient inside the cell were the main causes of inhomogeneous  $\text{Na}^+$  loss along the roll, as reflected in the composition of the recovered electrodes. Higher irreversibility was observed at the beginning of the roll (**Table 1**), and thus thicker SEI was expected on HC surface as higher temperatures were detected at the center of 18650 cells [45].

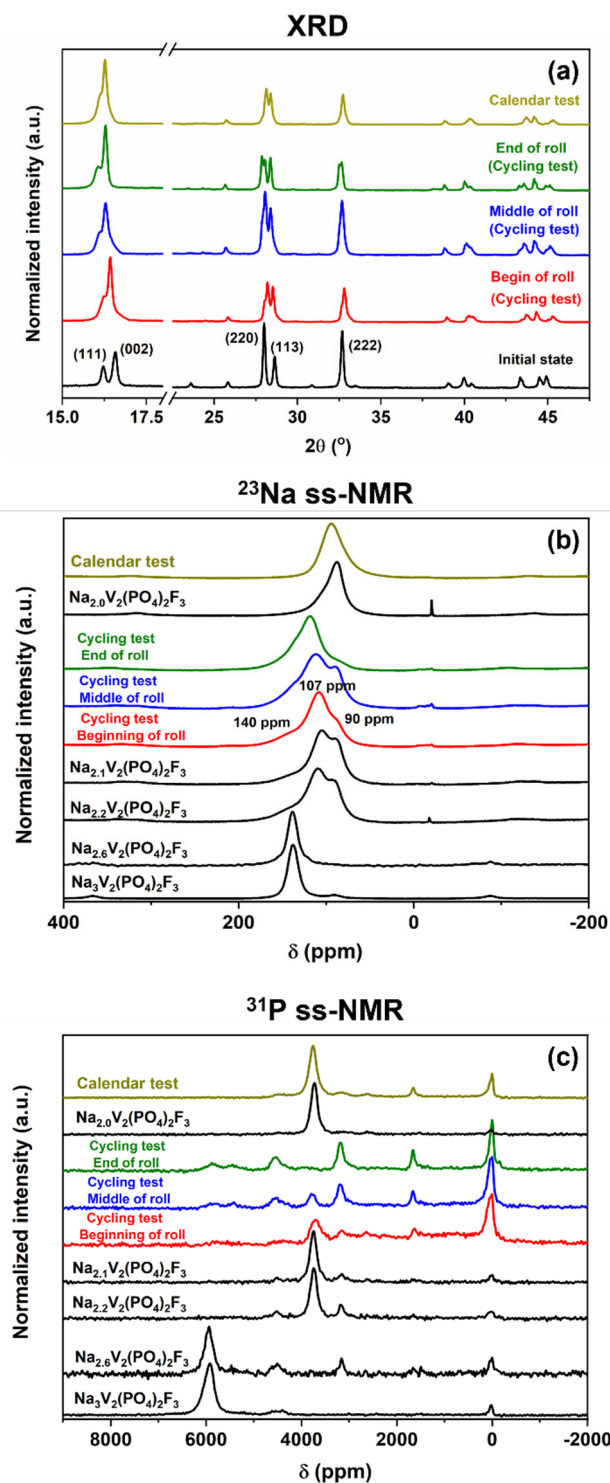


**Figure 5.** (a) XRD patterns corresponding to samples recovered at the beginning, the middle, and the end of the positive electrode after the long-term cycling test at 1C and 45°C compared to the one of the electrode recovered from the calendar test (middle of the roll). The XRD pattern of an uncycled  $\text{Na}_3\text{V}_2(\text{PO}_4)_2\text{F}_3$  electrode is given as a reference. (b)  $^{23}\text{Na}$  ss-NMR spectra recorded at  $B_0 = 11.7$  T with  $\nu_R = 30\text{kHz}$  of the aged electrodes as compared to those of  $\text{Na}_3\text{V}_2(\text{PO}_4)_2\text{F}_3$ ,  $\text{Na}_{2.6}\text{V}_2(\text{PO}_4)_2\text{F}_3$ ,  $\text{Na}_{2.2}\text{V}_2(\text{PO}_4)_2\text{F}_3$ ,  $\text{Na}_{2.1}\text{V}_2(\text{PO}_4)_2\text{F}_3$ , and  $\text{Na}_{2.0}\text{V}_2(\text{PO}_4)_2\text{F}_3$

references. (c)  $^{31}\text{P}$  ss-NMR spectra phases recorded at  $B_0 = 2.35$  T with  $\nu_R = 30$  kHz of the aged electrodes as compared to those of  $\text{Na}_3\text{V}_2(\text{PO}_4)_2\text{F}_3$ ,  $\text{Na}_{2.6}\text{V}_2(\text{PO}_4)_2\text{F}_3$ ,  $\text{Na}_{2.2}\text{V}_2(\text{PO}_4)_2\text{F}_3$ ,  $\text{Na}_{2.1}\text{V}_2(\text{PO}_4)_2\text{F}_3$ , and  $\text{Na}_{2.0}\text{V}_2(\text{PO}_4)_2\text{F}_3$  references.

The positive electrode recovered from the calendar test at  $45^\circ\text{C}$  was also analysed by XRD and the profile matching analysis revealed the presence of two different phases whose composition was close to  $\text{Na}_{2.0}\text{V}_2(\text{PO}_4)_2\text{F}_3$  (**Table 1** and **Figure S11**). Overall, it appears that whatever the cycling conditions, the compositional inhomogeneity seemed to occur from the very first cycles due to the loss of  $\text{Na}^+$  inventory resulting from the SEI formation. This loss seemed tremendous in the calendar test, where the cell was stored at 100% SoC during nearly four months, compared to the continuous long-term cycling test, likely related to more severe electrolyte decomposition under these conditions.

**Table 1.** Calculated cell parameters in the  $I4/mmm$  space group of  $\text{Na}_x\text{V}_2(\text{PO}_4)_2\text{F}_3$  compositions observed at different zones of the positive electrode recovered after the long-term cycling test at 1C and  $45^\circ\text{C}$ , and for the positive electrode recovered after the calendar test at  $45^\circ\text{C}$  (middle of roll). The cell parameters of  $\text{Na}_3\text{V}_2(\text{PO}_4)_2\text{F}_3$ ,  $\text{Na}_{2.2}\text{V}_2(\text{PO}_4)_2\text{F}_3$ , and  $\text{Na}_2\text{V}_2(\text{PO}_4)_2\text{F}_3$  [44] are used as reference to determine the Na-content in  $\text{Na}_x\text{V}_2(\text{PO}_4)_2\text{F}_3$ .

	$a$ (Å)	$b$ (Å)	$c$ (Å)	$V/Z$ (Å <sup>3</sup> )	
$\text{Na}_3\text{V}_2(\text{PO}_4)_2\text{F}_3^\dagger$	6.3843(1)	6.3941(1)	10.7402(5)	219.20(1)	
$\text{Na}_{2.2}\text{V}_2(\text{PO}_4)_2\text{F}_3$	6.3244(1)	6.3244(1)	10.7837(3)	215.66(1)	
$\text{Na}_2\text{V}_2(\text{PO}_4)_2\text{F}_3$	6.3021(1)	6.3021(1)	10.7933(2)	214.34(1)	
					Estimated composition
Position					
<b>Beginning of roll</b>	6.3273(3)	6.3273(3)	10.770(1)	215.59(1)	$\text{Na}_{2.2}\text{V}_2(\text{PO}_4)_2\text{F}_3$
	6.3256(3)	6.3256(3)	10.7855(5)	215.78(1)	" $\text{Na}_{2.3}\text{V}_2(\text{PO}_4)_2\text{F}_3$ "
<b>Middle of roll</b>	6.3365(4)	6.3365(4)	10.753(1)	215.87(1)	" $\text{Na}_{2.3}\text{V}_2(\text{PO}_4)_2\text{F}_3$ "
	6.3290(3)	6.3290(3)	10.7840(6)	215.98(1)	
<b>End of roll</b>	6.3557(8)	6.3557(8)	10.783(2)	217.78(1)	" $\text{Na}_{2.7}\text{V}_2(\text{PO}_4)_2\text{F}_3$ "
	6.3220(8)	6.3220(8)	10.782(2)	215.46(1)	$\text{Na}_{2.2}\text{V}_2(\text{PO}_4)_2\text{F}_3$
<b>Calendar test (middle of roll)</b>	6.3100(3)	6.3100(3)	10.781(1)	214.62(1)	$\text{Na}_{2.0}\text{V}_2(\text{PO}_4)_2\text{F}_3$
	6.3060(3)	6.3060(3)	10.7869(4)	214.47(1)	

$^\dagger$  From the crystallographic point of view, the structure of  $\text{Na}_3\text{V}_2(\text{PO}_4)_2\text{F}_3$  is described in the  $Amam$  space group with  $a = 9.02847(3)$  Å,  $b = 9.04444(3)$  Å, and  $c = 10.74666(6)$  Å. In this case, a cell transformation is applied to convert all the systems to the same setting in the  $I4/mmm$  space group for comparative purposes.

**$^{23}\text{Na}$  solid-state NMR spectroscopy.**  $^{23}\text{Na}$  ss-NMR spectra of samples recovered from the positive electrode at the beginning, middle, and end of the roll recovered from the long-term cycling were compared to those of  $\text{Na}_3\text{V}_2(\text{PO}_4)_2\text{F}_3$ ,  $\text{Na}_{2.6}\text{V}_2(\text{PO}_4)_2\text{F}_3$ ,  $\text{Na}_{2.2}\text{V}_2(\text{PO}_4)_2\text{F}_3$ ,  $\text{Na}_{2.1}\text{V}_2(\text{PO}_4)_2\text{F}_3$  and  $\text{Na}_{2.0}\text{V}_2(\text{PO}_4)_2\text{F}_3$  references in **Figure 5b**. The  $^{23}\text{Na}$  NMR spectrum of uncycled  $\text{Na}_3\text{V}_2(\text{PO}_4)_2\text{F}_3$  shows its main resonance at 139 ppm (**Figure 5b**), which is attributed to the Fermi contact between Na nuclei and the two neighboring  $\text{F}-\text{V}^{3+}\text{O}_4-\text{F}$  octahedral sites [23,46]. The  $^{23}\text{Na}$  NMR spectrum recorded on the  $\text{Na}_{2.6}\text{V}_2(\text{PO}_4)_2\text{F}_3$  reference was very similar to that of  $\text{Na}_3\text{V}_2(\text{PO}_4)_2\text{F}_3$ , implying a predominant presence of  $\text{V}^{3+}$  ions. For lower Na contents,  $\text{Na}_x\text{V}_2(\text{PO}_4)_2\text{F}_3$  ( $x = 2.2$  and  $2.1$ ) references, three  $^{23}\text{Na}$  resonances could be detected at 140 ppm, 107 ppm, and 90 ppm, which can be assigned to  $\text{Na}^+$  ions in  $\text{Na}(\text{V}^{3+}\text{O}_4\text{F}_2)_2$ ,  $\text{Na}(\text{V}^{3+}\text{O}_4\text{F}_2)(\text{V}^{4+}\text{O}_4\text{F}_2)$  and  $\text{Na}(\text{V}^{4+}\text{O}_4\text{F}_2)_2$  local environments, respectively [46].

The observed  $^{23}\text{Na}$  resonances were deconvoluted to determine the contribution of each component to the total signal (**Figure S12** and **Table S4**). These three  $^{23}\text{Na}$  NMR resonances were also recorded on samples recovered from different parts of the positive electrode after the long-term cycling test. The signal deconvolution analysis showed that the relative intensity between signals observed at the beginning and middle of the roll was quite similar to those observed in the  $\text{Na}_{2.2}\text{V}_2(\text{PO}_4)_2\text{F}_3$  reference (**Figure S12** and **Table S4**), which was in agreement with the  $\text{Na}_{2.2}\text{V}_2(\text{PO}_4)_2\text{F}_3$ – $\text{Na}_{2.3}\text{V}_2(\text{PO}_4)_2\text{F}_3$  compositional range as suggested by XRD analysis. Moreover, the  $^{23}\text{Na}$  NMR spectrum recorded at the end of the recovered electrode showed an important contribution (49%) of the resonance at 137 ppm, due to the Na-rich composition “ $\text{Na}_{2.7}\text{V}_2(\text{PO}_4)_2\text{F}_3$ ”, again in agreement with results from XRD.

On the other hand, the  $^{23}\text{Na}$  NMR spectrum of the positive electrode recovered from the calendar test shows two resonances at 95 and 84 ppm, which was quite similar to those of  $\text{Na}_{2.0}\text{V}_2(\text{PO}_4)_2\text{F}_3$  reference (**Figure S12** and **Table S4**); nonetheless, the contribution of the signal at 84 ppm observed in the recovered electrode was lower than in the  $\text{Na}_{2.0}\text{V}_2(\text{PO}_4)_2\text{F}_3$  reference (**Table S4**). This indicates the electrode recovered from the calendar test would have a composition in the range of  $\text{Na}_{2.0}\text{V}_2(\text{PO}_4)_2\text{F}_3$ – $\text{Na}_{2.1}\text{V}_2(\text{PO}_4)_2\text{F}_3$ .

**$^{31}\text{P}$  solid-state NMR spectroscopy.** The  $^{31}\text{P}$  ss-NMR spectra of the aged electrodes were compared to those of  $\text{Na}_3\text{V}_2(\text{PO}_4)_2\text{F}_3$ ,  $\text{Na}_{2.2}\text{V}_2(\text{PO}_4)_2\text{F}_3$ ,  $\text{Na}_{2.1}\text{V}_2(\text{PO}_4)_2\text{F}_3$ , and  $\text{Na}_{2.0}\text{V}_2(\text{PO}_4)_2\text{F}_3$  references in **Figure 5c**. The main resonance observed at 6000 ppm in the uncycled  $\text{Na}_3\text{V}_2(\text{PO}_4)_2\text{F}_3$  (**Figure 5c**) was due to the Fermi contact between the P nuclei and the four

neighboring  $V^{3+}$  in the  $P(V^{3+}O_4F_2)_4$  local environments [42,46], and there was no significant change in the position of the  $^{31}P$  signal when moving from  $Na_3V_2(PO_4)_2F_3$  to  $Na_{2.6}V_2(PO_4)_2F_3$ , as shown in **Figure 5c**. The  $^{31}P$  ss-NMR spectra of  $Na_{2.2}V_2(PO_4)_2F_3$  and  $Na_{2.1}V_2(PO_4)_2F_3$  look quite similar, and they both show resonances at 4500 ppm, 3700 ppm, and 3000 ppm, with the main one being that at 3700 ppm.

The  $^{31}P$  ss-NMR spectra recorded on different parts of the positive electrode recovered from the long-term cycling test showed several resonances at 6000 ppm, 4500 ppm, 3700 ppm, 1500 ppm, and 0 ppm, which did not resemble any reference. This long-term cycling electrode suffered several successive phase transitions coupled with a continuous electrode degradation process, and a combination of these factors could introduce several structural defects and the existence of several phosphorus local environments.  $^{31}P$  ss-NMR spectra of cycled electrodes showed several complicated resonances and deviated significantly from references; hence,  $^{31}P$  ss-NMR could hardly provide any explicit information on the composition of the long-term cycling electrode. Nonetheless, the apparent  $^{31}P$  resonances at 6000 and 5500 ppm observed at the end of the roll could be linked to the presence of  $V^{3+}$ -rich domains in the expected “ $Na_{2.7}V_2(PO_4)_2F_3$ ” composition. On the other hand, the  $^{31}P$  ss-NMR spectrum of the positive electrode recovered from the calendar test showed an intense signal at 3700 ppm (**Figure 5c**), which was very similar to the main resonance observed in the  $Na_{2.0}V_2(PO_4)_2F_3$  reference, again in full agreement with XRD results.

In order to complement to the characterisation of aged NVPF electrodes by bulk-sensitive techniques, the surface chemistry was investigated with the help of a surface-sensitive technique, namely XPS.

**X-ray photoelectron spectroscopy (XPS).** Both negative and positive electrodes recovered from the aging tests (long-term cycling and calendar tests) were analysed by XPS.

**Negative electrodes.** **Figure 6** displays V 2p, C 1s, and F 1s XPS spectra of the samples of the cycled negative electrode recovered after the calendar aging test from three different locations of the roll. O 1s, P 2p, and Na 2s spectra are also given as supplementary information in **Figure S13**. Quantification of all core peaks is provided in **Table S5**. Significant amount of vanadium was found on the surface of these negative HC electrodes after the cycling and calendar aging tests, as evidenced by V 2p spectra (**Figure 6a**). The global amount of vanadium was in the range of 1–2 at.% (atomic percentage) on three different roll locations for the cycled electrode and reached 3.3 at.% for the calendar aging. Three kinds of vanadium environments were

observed at the surface of the HC electrode, with three different V 2p<sub>3/2</sub> binding energies: 515.5, 516.5, and 517.5 eV. The highest one at 517.5 eV matched rather well with V<sup>3+</sup> from NVPF; however, NVPF structure was not expected to be found at the surface of the negative electrode after its partial dissolution and migration/diffusion of the dissolved vanadium through the electrolyte. This binding energy also matched well with V<sup>5+</sup> from V<sub>2</sub>O<sub>5</sub>, and the two other observed binding energies, 515.5 and 516.5 eV, were in good agreement with V<sup>3+</sup> and V<sup>4+</sup> from V<sub>2</sub>O<sub>3</sub> and V<sub>2</sub>O<sub>4</sub> [47,48]. Therefore, the presence of vanadium at these three different oxidation states could be explained by the electrochemical reduction of the dissolved vanadium into V<sup>0</sup> at the negative electrode surface at low potential and its oxidation after deposition. The oxidation of V<sup>0</sup> could be triggered by oxygen traces or even solvent molecules due to the high reactivity of the electrodeposited vanadium as metallic nanoparticles. This amount of vanadium could enhance the electronic conductivity of the SEI (which should ideally remain electronically insulating) or its chemical instability. This metal content is in the range of the values reported for LIBs. For instance, 0.9 at.% of Co was observed at the surface of the graphite electrode of a graphite||LiCoO<sub>2</sub> full-cell after only 60 cycles between 2.7 and 4.4 V with LiPF<sub>6</sub> salt [49]. Therefore, 1–2 at.% of vanadium, observed on the surface of our HC electrode after 800 cycles between 2.0 and 4.25V (harder oxidising conditions), is not likely to play a detrimental role on the SEI stability.

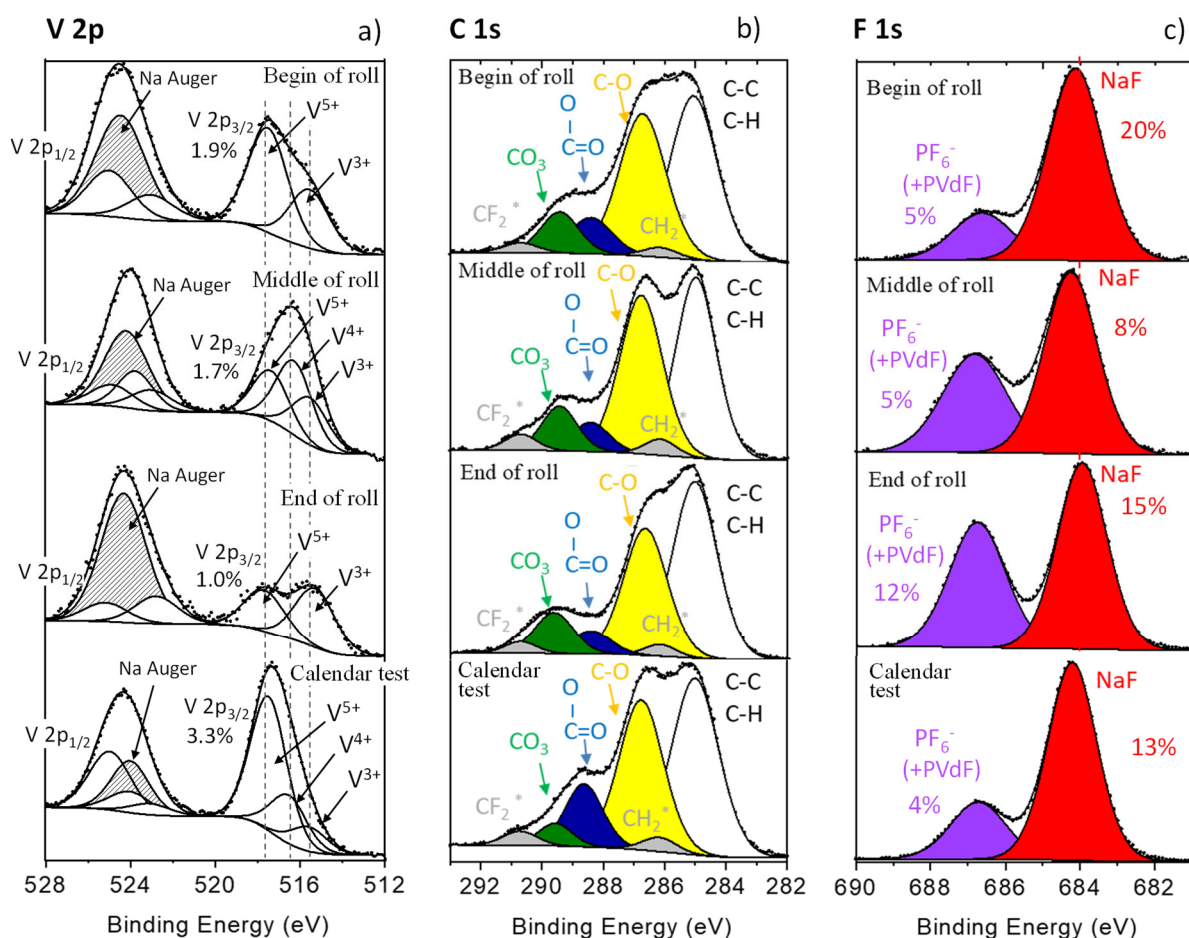


**Figure 6.** XPS (a) V 2p, (b) C 1s, and (c) F 1s spectra of HC samples recovered from different locations of the negative electrode after long-term cycling at 45°C and after the calendar aging. Na Auger peaks overlapping with V 2p spectra correspond to the Na KL<sub>1</sub>L<sub>2,3</sub> (<sup>3</sup>P) transition. The CH<sub>2</sub>\* and CF<sub>2</sub>\* contributions in C 1s spectra correspond to the PVdF binder.

C 1s and F 1s peaks (**Figures 6b** and **6c**) provided helpful information on the chemical composition of the SEI. First of all, for none of these four samples, the C 1s signal of the HC active material could be detected after aging, which means that the SEI thickness was more significant than the probing depth of XPS at the usual photon energy (~ 5-10 nm for  $h\nu = 1486.6$  eV). Moving the photon energy up to  $h\nu = 2984.2$  eV (with the Ag L $\alpha$  source available on the same machine) did not allow to reach the C 1s signal of the HC, although the probing depth was about twice greater at this energy. The observed C 1s components were characteristic of the various carbon environments of species in the SEI: the 285.0 eV binding energy corresponds to C atoms linked only to H and C atoms, related to aliphatic chains and natural hydrocarbon surface contamination, as usually observed in XPS spectra. The contribution at 286.6–286.8 eV

was attributed to C atoms bound to one oxygen (yellow component), the one at 288.4–288.6 eV was assigned to O–C=O environments (blue), and the one at 289.4–289.6 eV was due to CO<sub>3</sub> carbonate environments (green). The weak component at higher binding energy (290.6–290.7 eV) was attributed to CF<sub>2</sub> groups of PVdF binder (grey component). To fully account for the contribution of PVdF binder, an additional component at 286.1 eV corresponding to CH<sub>2</sub> groups of PVdF was included in the fitting and constrained to be equal to the CF<sub>2</sub> component in width and intensity. It appears that C 1s spectra of the three different roll locations after long cycling were quite similar, showing that the composition in carbonaceous species in the SEI was relatively homogeneous in the whole electrode (which was also confirmed by O 1s spectra, **Figure S13a**). Concerning the electrode obtained after calendar aging, we can notice a smaller amount of carbonates and a greater content of O=C–O environments (**Table S5**).

The amount of inorganic species fluctuated greatly, as shown by F 1s spectra in **Figure 6c** (and also P 2p spectra in **Figure S13b**). F 1s spectra displayed a first (purple) component at  $\approx 687$  eV corresponding to PF<sub>6</sub><sup>-</sup> anions in the SEI and the PVdF binder, and a second (red) component at  $\approx 684$  eV corresponding to NaF generated by the degradation of both NaPF<sub>6</sub> salt and FEC additive. The measured amount of NaF (at.% of NaF = at.% of F + at.% of Na = 2 × at.% of F at 684 eV) accounts for 16 to 40 at.% of the SEI surface composition for the four samples (cycling and calendar aging). Phosphates originating from salt degradation were also detected.

As a summary, it is interesting to note for all negative electrodes that the amount of carbonates, commonly due to Na<sub>2</sub>CO<sub>3</sub> or sodium alkyl carbonates like sodium ethylene dicarbonate (SEDC), was low compared to other studies using similar solvents and/or salts [36,38,50] performed in electrodes recovered from half-cells. NaF being known as a poor ionic conductor contrary to other Na-rich species like SEDC, the presence of this compound in high quantity in the SEI might contribute to the capacity fading observed in these electrodes.

**Positive electrodes.** **Figure 7** presents V 2p, V 3p, valence (V 3d), and P 2p XPS spectra of the uncycled NVPF positive electrode compared with the one recovered from three different locations of the electrode after cycling and after the calendar aging test. C 1s, O 1s, and F 1s spectra are given in **Figure 8**. Quantification of all core peaks is provided in **Table S6**. The maximum position in V 2p spectra recorded on recovered electrodes did not change significantly compared to the uncycled NVPF electrode (**Figure 7a**), implying that vanadium recovered the +3 oxidation state. This observation contradicted NMR and XRD results showing

that Na was not fully reinserted into the NVPF electrode in the cycling and calendar tests. However, the V 2p binding energy depends on the local environment of vanadium and the crystalline structure, and for example,  $V^{3+}$  in NVPF has about the same binding energy as  $V^{5+}$  in  $V_2O_5$ . Moreover, we know that because of partial dissolution of NVPF, one or several other vanadium-containing compounds may be present at the surface of the positive electrodes. Therefore, the V 2p probe alone was insufficient to investigate vanadium oxidation states correctly.

V 3p/V 3d intensity ratio in XPS can be used as an alternative to identify vanadium oxidation states. A slight V 3d peak could be identified at  $\sim 2$  eV close to the Fermi level in the valence spectrum (**Figure 7b**). The intensity of this V 3d peak is proportional to the number of 3d electrons, and thus vanadium oxidation state:  $3d^2$  ( $V^{3+}$ ),  $3d^1$  ( $V^{4+}$ ), and  $3d^0$  ( $V^{5+}$ ), while the one of V 3p peak does not vary as a function of 3d electron number. It is thus possible to calculate the average vanadium oxidation state on the surface of the electrodes from the V 3p/V 3d intensity ratio by comparison with the same ratio measured on the uncycled electrode. The result of this analysis gave the following average vanadium oxidation states: beginning of roll +3.2, middle of roll +3.7, end of roll +3.3, and calendar aging +3.7. This heterogeneity between the different parts of the same cycled electrode (beginning, middle and end) is fully consistent with the results from XRD and NMR studies.

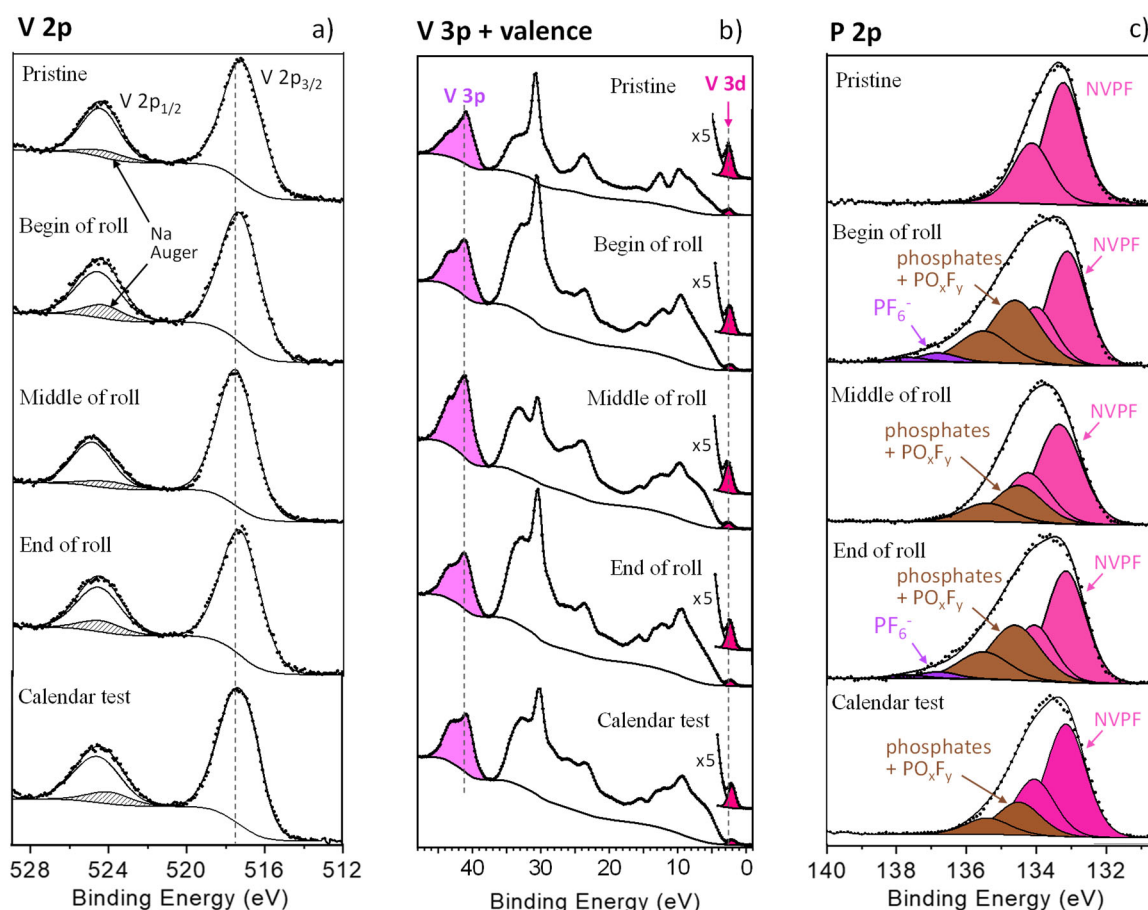


**Figure 7.** (a) V 2p, (b) V 3p + valence and (c) P 2p XPS spectra of NVPF samples recovered from different locations of positive electrode after long-term cycling at 45°C and after the calendar aging, compared with the uncycled composite electrode. Na Auger peaks overlapping with V 2p spectra correspond to the Na KL<sub>1</sub>L<sub>2,3</sub> (<sup>3</sup>P) transition.

P 2p spectra show the signature of (PO<sub>4</sub>)<sup>3-</sup> groups of NVPF (133.1–133.2 eV), together with another P 2p signature appearing at 134.5–134.6 eV, which was significantly higher than the phosphates originated from salt degradation (as observed at the surface of the negative electrode). This component could be linked to surface attack of the NVPF material, leading to vanadium dissolution and release of undefined phosphates or PO<sub>x</sub>F<sub>y</sub> species and might explain some unidentified peaks in <sup>31</sup>P ss-NMR spectra. Phosphates originating from salt degradation might also be present on the surface of the positive electrode and overlap with other signals. Finally, a weak P 2p signature of the salt NaPF<sub>6</sub> was observed for two samples.

The C 1s and F 1s spectra of the positive electrode (**Figures 8a** and **8b**) were dominated by PVdF binder and carbon Super P. However, the C 1s spectra of aged electrodes display some

differences compared to uncycled NVPF electrode, with the appearance of different oxygenated environments of carbon corresponding to deposited organic species on the surface of the electrode, ensuing from carbonate solvents degradation. As observed on the HC negative electrodes, the surface reactivity seemed to be enhanced by calendar aging at 100 % SoC.

The O 1s signature of  $(\text{PO}_4)^{3-}$  groups of NVPF was still observed after cycling and calendar aging (black peak on **Figure 8c**). Two new components were also observed (brown and yellow peaks at 532 and 533.7 eV, respectively), which could be assigned to oxygenated organic species detected in C 1s spectra and surface degradation species, in agreement with P 2p spectra. For all samples, the amount of inorganic deposited species was lower than observed at the surface of the negative electrodes: the presence of NaF could not be demonstrated since the intensity of the F 1s peak at 684 eV did not significantly increase after aging, and neither did the Na Auger peaks in O 1s and V 2p spectra.

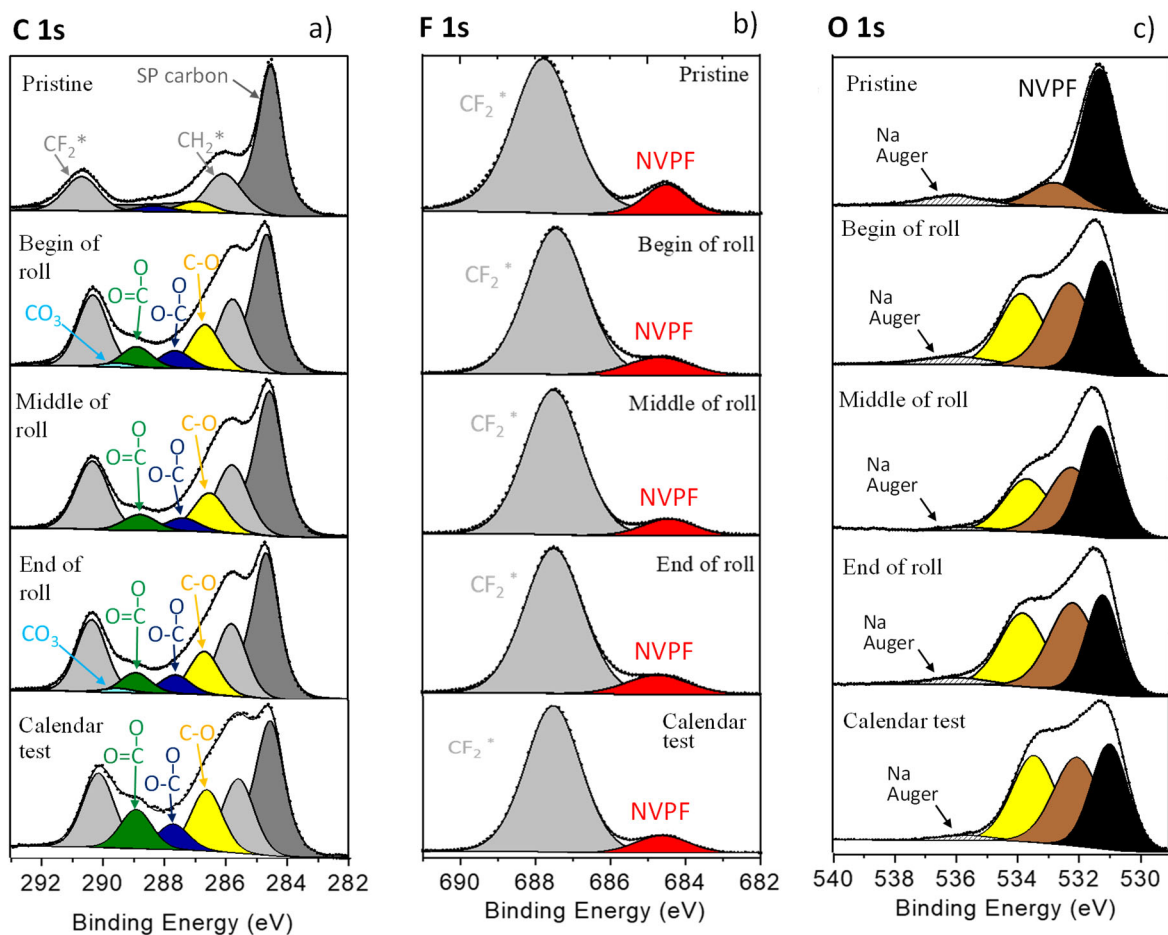


**Figure 8.** (a) C 1s, (b) F 1s, and (c) O 1s XPS spectra of NVPF samples recovered from different locations of the positive electrode after long-term cycling at 45°C and after the calendar aging, compared with the uncycled NVPF electrode. Na Auger peaks overlapping with O 1s spectra correspond to the Na  $\text{KL}_1\text{L}_{2,3}$  ( $^1\text{P}_1$ ) transition.

#### 4. Global discussions

Overall, the aging process in Hard carbon||Na<sub>3</sub>V<sub>2</sub>(PO<sub>4</sub>)<sub>2</sub>F<sub>3</sub> full-cells in the 18650-format occurs via several mechanisms: loss of Na inventory in irreversible capacity and SEI formation, loss of vanadium in NVPF electrode through dissolution and deposition on the negative electrode, electrolyte decomposition, and internal resistance build-up. These phenomena seem to be promoted by elevated temperatures, cycling at low C rates (or during a long time), and long rest periods at high SoCs, which is consistent with the current knowledge of aging in LIBs.

Indeed, degradation mechanisms observed at the positive electrode in LIBs are commonly classified into (i) loss of Li<sup>+</sup> ions that are no longer available to shuttle between the two electrodes and (ii) loss of active material in the electrode [1,3,4,6,51]. Both mechanisms were observed in this study; nonetheless, the loss of Na inventory was found to be predominant, the main cause being the consumption of Na<sup>+</sup> ions in the formation of the SEI layer on HC electrode. Some previous studies on LIBs pointed out that Li<sup>+</sup> loss could also be rooted in the Li plating process [6], which was not the case for Na<sup>+</sup> in this study.

The capacity degradation can also come from a loss of the active material in the electrode through a “dissolution–migration–catalytic reduction” process [6,52,53]. The dissolution of transition metal ions is often assigned to acid attack, with the main dissolving agent being HF, which is a product coming from the hydrolysis of PF<sub>6</sub><sup>-</sup>. The dissolved ions can thus migrate through the separator and deposit on the negative electrode. The low amount of vanadium deposited on HC electrode found in this study (1–2 at.%) seems to indicate that NVPF would be relatively resistant to the acidic corrosion. Yet, further studies are still required to fully understand the involved processes.

On the other hand, it has already been demonstrated for 18650 Li-ion cells using graphite electrodes that one of the main reasons behind capacity loss is the SEI thickening upon cycling [34]. In the present case, due to the higher solubility of Na salts when compared with their Li analogues, the evolution of the SEI upon time/cycling is expected to be more drastic [36,54]. Upon dissolution of the Na-based SEI components, the passivating role of this layer can be lost, resulting in further electrolyte reduction. This process can occur during rest periods at high SoCs or upon cycling at low C rates when more time is allowed during each cycle for SEI dissolution. These effects can eventually thicken the passivation layer and modify its composition with an increased proportion of the most insoluble compounds (such as NaF).

These assumptions are in full agreement with results from XPS measurements, which enable to conclude that a rather thick SEI is formed (> 20 nm since hard carbon cannot be detected using

$h\nu = 2984.2$  eV). The detected NaF content (between 16 and 40 at.% at the electrode surface), is significantly higher than what could be measured in Na half-cells after about 100 cycles ( $\sim 5$  at.%, see [38]). These observations and the increase in the cell's internal resistance upon time reveal that SEI layers in HC||NVPF full-cells evolve towards less soluble/inorganic components during cycling with a significant content of NaF, which is a poor ionic and electronic conductor. One can hence infer that SEI dissolution and regrowth can be one of the main origins for the loss of Na inventory deduced from post-mortem analysis of NVPF electrodes. Indeed, upon calendar test, the SEI reformation can occur without current flowing between the electrodes (open circuit voltage, OCV) through the electrolyte reduction concomitantly with the oxidation of hard carbon ( $\text{Na}^+$  removal). This loss of Na will eventually lead to capacity loss and incomplete  $\text{Na}^+$  re-insertion into NVPF. Upon continuous cycling, the SEI dissolution and reformation occur continuously via a gradual consumption of  $\text{Na}^+$  inventory in the positive electrode and an increase of irreversible capacity. Compared with aging upon continuous cycling, the more substantial capacity loss recorded for the calendar test at 100% SoC suggests that OCV period could favour the SEI dissolution and reformation on the HC electrode. Indeed,  $\text{Na}^+$  insertion into HC and the electrolyte reduction are competing redox processes upon cycling, while only electrolyte reduction can occur during OCV period due to direct contact between the electrolyte and the fully charged electrodes.

Temperature is an important parameter affecting the SEI dissolution and reformation. More severe loss of Na inventory from the positive electrode and a higher increase in the cell's internal resistance were observed at more elevated temperatures. In 18650-format cells, a temperature gradient exists with a higher temperature detected in the inner part of the cell [45]. This phenomenon explains why an inhomogeneity in  $\text{Na}^+$  loss is observed at different parts of the NVPF roll. Furthermore, SEI dissolution and reformation are more critical at the inner part of the cell, where a higher temperature was reported. The SEI layer observed on the HC electrode at the cell core is rich in NaF content (about 40 at.%).

Finally, mechanical stresses could be observed at the electrode level for cells aged through long-term cycling (folding of the separators, see **Figure 4**), while no such evidence could be seen after dismantling cells after calendar aging at high SoC (**Figure S5**). Nevertheless, the capacity loss and internal resistance build-up in calendar aging are more severe than long-term cycling aging. These observations indicate that irreversible capacity loss due to  $\text{Na}^+$  consumption in the SEI dissolution and regrow is the most problematic aging mechanism in Na cells compared with other issues such as mechanical stress build-up or particle disconnection.

## 5. Conclusions

Thirty-six HC||NVPF full-cells in 18650-format were successfully assembled, and all the cells exhibited identical electrochemical performance. The assembled cells underwent aging tests at continuous cycling or storage at elevated temperatures (calendar test). The obtained results reveal that temperature is the primary factor impacting cell degradation and capacity loss. The cell aging process was more pronounced at low current rates in continuous cycling conditions as the electrolyte decomposition was more important. Furthermore, the continuous sodiation/desodiation likely induces mechanical stress, leading to the folding of the jelly rolls in the middle of the cell and the detachment of the active materials from the current collector, a phenomenon not observed after calendar ageing. In calendar test, degradation was found to be more significant at high SoC due to the high open-circuit voltage of the cells, causing enhanced electrolyte decomposition due to direct contact with the very oxidising/reducing nature of the positive/negative electrode surfaces, respectively.

By combining XRD,  $^{23}\text{Na}$ , and  $^{31}\text{P}$  ss-NMR, we demonstrated that NVPF structure can withstand long-term cycling, even at elevated temperature ( $45^\circ\text{C}$ ), despite significant capacity loss caused by the loss of Na inventory associated to SEI formation on the HC electrode. Inhomogeneity in the Na content throughout the electrode occurred from the first cycles, its extent depending on the internal pressure/temperature gradient being enhanced at the centre of the cell, where higher temperature is expected. SEI dissolution and reformation was identified as one of the most a critical parameter with respect to aging mechanisms. The high solubility of some Na based SEI components eventually results in its thickening and enrichment in NaF upon time and cycling.

XPS evidenced the formation of a relatively thick passivating layer on the surface of the negative electrode, its composition being analogous to those observed in LIBs. Deposited species were also observed on the positive electrode but to a much lesser extent. In both cases, the phenomenon is more significant after calendar aging at 100% SoC than during long-term cycling. Finally, XPS studies also enabled to detect a slight dissolution of vanadium from the positive electrode, which would end up deposited on the surface of the negative electrode. Despite the process being enhanced during calendar aging at 100% SoC, the observed dissolution level is low and acceptable for practical use in batteries.

## Acknowledgements

The authors acknowledge the European Commission for funding this work through the H2020 NAIADES project (LCE10-2014, Contract number 646433). LC, DC, PSC and LHBN thank the RS2E Network for the funding of LHBN's PhD thesis as well as the financial support of Région Nouvelle Aquitaine. LC, DC, PSC, LHBN, CC, and RD acknowledge the French National Research Agency (STORE-EX Labex Project ANR-10-LABX-76-01) for financial support. MRP and AP acknowledge Ministerio de Economía y Competitividad (Spain) for Severo Ochoa Programme for Centres of Excellence in R&D (SEV-2015-0496). The authors thank E. Garitte (SAFT, France) for her helps to coordinate this project.

## References

- [1] M.R. Palacín, A. De Guibert, Batteries: Why do batteries fail?, *Science* (80-. ). 351 (2016). <https://doi.org/10.1126/science.1253292>.
- [2] P. Arora, E.W. Ralph, D. Marc, Capacity Fade Mechanisms and Side Reactions in Lithium-Ion Batteries, *J. Electrochem. Soc.* 145 (1998) 3647. <https://doi.org/10.1149/1.1838857>.
- [3] M. Broussely, P. Biensan, F. Bonhomme, P. Blanchard, S. Herreyre, K. Nechev, R.J. Staniewicz, Main aging mechanisms in Li ion batteries, *J. Power Sources.* 146 (2005) 90–96. <https://doi.org/10.1016/j.jpowsour.2005.03.172>.
- [4] J. Vetter, P. Novák, M.R. Wagner, C. Veit, K.C. Möller, J.O. Besenhard, M. Winter, M. Wohlfahrt-Mehrens, C. Vogler, A. Hammouche, Ageing mechanisms in lithium-ion batteries, *J. Power Sources.* 147 (2005) 269–281. <https://doi.org/10.1016/j.jpowsour.2005.01.006>.
- [5] C.R. Birkel, M.R. Roberts, E. McTurk, P.G. Bruce, D.A. Howey, Degradation diagnostics for lithium ion cells, *J. Power Sources.* 341 (2017) 373–386. <https://doi.org/10.1016/j.jpowsour.2016.12.011>.
- [6] M.R. Palacín, Understanding ageing in Li-ion batteries: A chemical issue, *Chem. Soc. Rev.* 47 (2018) 4924–4933. <https://doi.org/10.1039/c7cs00889a>.
- [7] T. Waldmann, B.I. Hogg, M. Wohlfahrt-Mehrens, Li plating as unwanted side reaction in commercial Li-ion cells – A review, *J. Power Sources.* 384 (2018) 107–124. <https://doi.org/10.1016/j.jpowsour.2018.02.063>.
- [8] N. Yabuuchi, K. Kubota, M. Dahbi, S. Komaba, Research development on sodium-ion batteries, *Chem. Rev.* 114 (2014) 11636–11682. <https://doi.org/10.1021/cr500192f>.
- [9] A. Ponrouch, D. Monti, A. Boschini, B. Steen, P. Johansson, M.R. Palacín, Non-aqueous electrolytes for sodium-ion batteries, *J. Mater. Chem. A.* 3 (2015) 22–42. <https://doi.org/10.1039/c4ta04428b>.
- [10] P. Johansson, P. Rozier, M. Rosa Palacín, Na-Ion Batteries — State of the Art and Prospects, in: *WORLD SCIENTIFIC*, 2018: pp. 161–235. [https://doi.org/10.1142/9789813228146\\_0004](https://doi.org/10.1142/9789813228146_0004).
- [11] I. Hasa, S. Mariyappan, D. Saurel, P. Adelhelm, A.Y. Kuposov, C. Masquelier, L. Croguennec, M. Casas-Cabanas, Challenges of today for Na-based batteries of the future: From materials to cell metrics, *J. Power Sources.* 482 (2021) 228872. <https://doi.org/10.1016/j.jpowsour.2020.228872>.
- [12] B. Jache, P. Adelhelm, Use of graphite as a highly reversible electrode with superior cycle life for sodium-ion batteries by making use of co-intercalation phenomena, *Angew. Chemie - Int. Ed.* 53 (2014) 10169–10173. <https://doi.org/10.1002/anie.201403734>.
- [13] E. Irisarri, A. Ponrouch, M.R. Palacín, Review—Hard Carbon Negative Electrode Materials for Sodium-Ion Batteries, *J. Electrochem. Soc.* 162 (2015) A2476–A2482. <https://doi.org/10.1149/2.0091514jes>.
- [14] V. Simone, A. Boulineau, A. de Geyer, D. Rouchon, L. Simonin, S. Martinet, Hard carbon derived from cellulose as anode for sodium ion batteries: Dependence of electrochemical properties on structure, *J. Energy Chem.* 25 (2016) 761–768. <https://doi.org/10.1016/j.jechem.2016.04.016>.
- [15] E. Irisarri, N. Amini, S. Tennison, C.M. Ghimbeu, J. Gorka, C. Vix-Guterl, A. Ponrouch, M.R. Palacín, Optimization of Large Scale Produced Hard Carbon Performance in Na-Ion Batteries: Effect of Precursor, Temperature and Processing Conditions, *J. Electrochem. Soc.* 165 (2018) A4058–A4066.

<https://doi.org/10.1149/2.1171816jes>.

[16] C. Vaalma, D. Buchholz, M. Weil, S. Passerini, A cost and resource analysis of sodium-ion batteries, *Nat. Rev. Mater.* 3 (2018) 18013. <https://doi.org/10.1038/natrevmats.2018.13>.

[17] C.D. Wessells, Batteries Containing Prussian Blue Analogue Electrodes, in: *Na-ion Batter.*, Wiley, 2021: pp. 265–311. <https://doi.org/10.1002/9781119818069.ch7>.

[18] A. Rudola, F. Coowar, R. Heap, J. Barker, The Design, Performance and Commercialization of Faradion's Non-aqueous Na-ion Battery Technology, in: *Na-ion Batter.*, Wiley, 2021: pp. 313–344. <https://doi.org/10.1002/9781119818069.ch8>.

[19] A. Rudola, A.J.R. Rennie, R. Heap, S.S. Meysami, A. Lowbridge, F. Mazzali, R. Sayers, C.J. Wright, J. Barker, Commercialisation of high energy density sodium-ion batteries: Faradion's journey and outlook, *J. Mater. Chem. A* 9 (2021) 8279–8302. <https://doi.org/10.1039/d1ta00376c>.

[20] A. Ponrouch, R. Dedryvere, D. Monti, A.E. Demet, J.M. Ateba Mba, L. Croguennec, C. Masquelier, P. Johansson, M.R. Palacin, Towards high energy density sodium ion batteries through electrolyte optimization, *Energy Environ. Sci.* 6 (2013) 2361–2369. <https://doi.org/10.1039/c3ee41379a>.

[21] R. Dugas, B. Zhang, P. Rozier, J.M. Tarascon, Optimization of Na-Ion Battery Systems Based on Polyanionic or Layered Positive Electrodes and Carbon Anodes, *J. Electrochem. Soc.* 163 (2016) A867–A874. <https://doi.org/10.1149/2.0051605jes>.

[22] T. Broux, F. Fauth, N. Hall, Y. Chatillon, M. Bianchini, T. Bamine, J.B. Leriche, E. Suard, D. Carlier, Y. Reynier, L. Simonin, C. Masquelier, L. Croguennec, High Rate Performance for Carbon-Coated  $\text{Na}_3\text{V}_2(\text{PO}_4)_2\text{F}_3$  in Na-Ion Batteries, *Small Methods* 3 (2019) 1800215. <https://doi.org/10.1002/smt.201800215>.

[23] Y.U. Park, D.H. Seo, H. Kim, J. Kim, S. Lee, B. Kim, K. Kang, A family of high-performance cathode materials for Na-ion batteries,  $\text{Na}_3(\text{VO}_{1-x}\text{PO}_4)_2\text{F}_{1+2x}$  ( $0 \leq x \leq 1$ ): Combined first-principles and experimental study, *Adv. Funct. Mater.* 24 (2014) 4603–4614. <https://doi.org/10.1002/adfm.201400561>.

[24] P. Serras, V. Palomares, A. Goñi, I. Gil de Muro, P. Kubiak, L. Lezama, T. Rojo, High voltage cathode materials for Na-ion batteries of general formula  $\text{Na}_3\text{V}_2\text{O}_{2x}(\text{PO}_4)_2\text{F}_{3-2x}$ , *J. Mater. Chem.* 22 (2012) 22301. <https://doi.org/10.1039/c2jm35293a>.

[25] W. Waag, S. Käbitz, D.U. Sauer, Experimental investigation of the lithium-ion battery impedance characteristic at various conditions and aging states and its influence on the application, *Appl. Energy* 102 (2013) 885–897. <https://doi.org/10.1016/j.apenergy.2012.09.030>.

[26] M. Ecker, J.B. Gerschler, J. Vogel, S. Käbitz, F. Hust, P. Dechent, D.U. Sauer, Development of a lifetime prediction model for lithium-ion batteries based on extended accelerated aging test data, *J. Power Sources* 215 (2012) 248–257. <https://doi.org/10.1016/j.jpowsour.2012.05.012>.

[27] M. Ecker, N. Nieto, S. Käbitz, J. Schmalstieg, H. Blanke, A. Warnecke, D.U. Sauer, Calendar and cycle life study of  $\text{Li}(\text{NiMnCo})\text{O}_2$ -based 18650 lithium-ion batteries, *J. Power Sources* 248 (2014) 839–851. <https://doi.org/10.1016/j.jpowsour.2013.09.143>.

[28] S. Käbitz, J.B. Gerschler, M. Ecker, Y. Yurdagel, B. Emmermacher, D. André, T. Mitsch, D.U. Sauer, Cycle and calendar life study of a graphite| $\text{LiNi}_{1/3}\text{Mn}_{1/3}\text{Co}_{1/3}\text{O}_2$  Li-ion high energy system. Part A: Full cell characterization, *J. Power Sources* 239 (2013) 572–583. <https://doi.org/10.1016/j.jpowsour.2013.03.045>.

[29] A. Farmann, W. Waag, A. Marongiu, D.U. Sauer, Critical review of on-board capacity estimation techniques for lithium-ion batteries in electric and hybrid electric vehicles, *J. Power Sources* 281 (2015) 114–130. <https://doi.org/10.1016/j.jpowsour.2015.01.129>.

[30] G. Liu, M. Ouyang, L. Lu, J. Li, X. Han, Online estimation of lithium-ion battery remaining discharge capacity through differential voltage analysis, *J. Power Sources* 274 (2015) 971–989. <https://doi.org/10.1016/j.jpowsour.2014.10.132>.

[31] G. Liu, M. Ouyang, L. Lu, J. Li, X. Han, Analysis of the heat generation of lithium-ion battery during charging and discharging considering different influencing factors, *J. Therm. Anal. Calorim.* 116 (2014) 1001–1010. <https://doi.org/10.1007/s10973-013-3599-9>.

[32] A. Cordoba-Arenas, S. Onori, Y. Guezennec, G. Rizzoni, Capacity and power fade cycle-life model for plug-in hybrid electric vehicle lithium-ion battery cells containing blended spinel and layered-oxide positive electrodes, *J. Power Sources* 278 (2015) 473–483. <https://doi.org/10.1016/j.jpowsour.2014.12.047>.

[33] M. Fleischhammer, T. Waldmann, G. Bisle, B.-I. Hogg, M. Wohlfahrt-Mehrens, Interaction of cyclic ageing at high-rate and low temperatures and safety in lithium-ion batteries, *J. Power Sources* 274 (2015) 432–439. <https://doi.org/10.1016/j.jpowsour.2014.08.135>.

[34] T. Waldmann, M. Wilka, M. Kasper, M. Fleischhammer, M. Wohlfahrt-Mehrens, Temperature dependent ageing mechanisms in Lithium-ion batteries – A Post-Mortem study, *J. Power Sources* 262 (2014) 129–135.

<https://doi.org/10.1016/j.jpowsour.2014.03.112>.

[35] T. Waldmann, M. Kasper, M. Wohlfahrt-Mehrens, Optimization of Charging Strategy by Prevention of Lithium Deposition on Anodes in high-energy Lithium-ion Batteries – Electrochemical Experiments, *Electrochim. Acta.* 178 (2015) 525–532. <https://doi.org/10.1016/j.electacta.2015.08.056>.

[36] D.I. Iermakova, R. Dugas, M.R. Palacín, A. Ponrouch, On the Comparative Stability of Li and Na Metal Anode Interfaces in Conventional Alkyl Carbonate Electrolytes, *J. Electrochem. Soc.* 162 (2015) A7060–A7066. <https://doi.org/10.1149/2.0091513jes>.

[37] R. Dugas, A. Ponrouch, G. Gachot, R. David, M.R. Palacin, J.M. Tarascon, Na Reactivity toward Carbonate-Based Electrolytes: The Effect of FEC as Additive, *J. Electrochem. Soc.* 163 (2016) A2333–A2339. <https://doi.org/10.1149/2.0981610jes>.

[38] J. Fondard, E. Irisarri, C. Courrèges, M.R. Palacin, A. Ponrouch, R. Dedryvère, SEI Composition on Hard Carbon in Na-Ion Batteries After Long Cycling: Influence of Salts (NaPF<sub>6</sub>, NaTFSI) and Additives (FEC, DMCF), *J. Electrochem. Soc.* 167 (2020) 070526. <https://doi.org/10.1149/1945-7111/ab75fd>.

[39] N. Hall, S. Boulineau, S. Launois, L. Simonin, L. Croguennec, C. Masquelier, Method for preparing a Na<sub>3</sub>V<sub>2</sub>(PO<sub>4</sub>)<sub>2</sub>F<sub>3</sub> particulate material, International Patent WO 2017/064189 A1, 2017.

[40] J. Rodríguez-Carvajal, Recent advances in magnetic structure determination by neutron powder diffraction, *Phys. B Condens. Matter.* 192 (1993) 55–69. [https://doi.org/10.1016/0921-4526\(93\)90108-I](https://doi.org/10.1016/0921-4526(93)90108-I).

[41] D. Massiot, F. Fayon, M. Capron, I. King, S. Le Calvé, B. Alonso, J. Durand, B. Bujoli, Z. Gan, G. Hoatson, Modelling one- and two-dimensional solid-state NMR spectra, *Magn. Reson. Chem.* 40 (2002) 70–76. <https://doi.org/10.1002/mrc.984>.

[42] T. Broux, T. Bamine, F. Fauth, L. Simonelli, W. Olszewski, C. Marini, M. Ménétrier, D. Carlier, C. Masquelier, L. Croguennec, Strong Impact of the Oxygen Content in Na<sub>3</sub>V<sub>2</sub>(PO<sub>4</sub>)<sub>2</sub>F<sub>3-y</sub> (0 ≤ y ≤ 0.5) on Its Structural and Electrochemical Properties, *Chem. Mater.* 28 (2016) 7683–7692. <https://doi.org/10.1021/acs.chemmater.6b02659>.

[43] L.H.B. Nguyen, T. Broux, P.S. Camacho, D. Denux, L. Bourgeois, S. Belin, A. Iadecola, F. Fauth, D. Carlier, J. Olchowka, C. Masquelier, L. Croguennec, Stability in water and electrochemical properties of the Na<sub>3</sub>V<sub>2</sub>(PO<sub>4</sub>)<sub>2</sub>F<sub>3</sub>–Na<sub>3</sub>(VO)<sub>2</sub>(PO<sub>4</sub>)<sub>2</sub>F solid solution, *Energy Storage Mater.* 20 (2019) 324–334. <https://doi.org/10.1016/j.ensm.2019.04.010>.

[44] M. Bianchini, F. Fauth, N. Brisset, F. Weill, E. Suard, C. Masquelier, L. Croguennec, Comprehensive Investigation of the Na<sub>3</sub>V<sub>2</sub>(PO<sub>4</sub>)<sub>2</sub>F<sub>3</sub>–NaV<sub>2</sub>(PO<sub>4</sub>)<sub>2</sub>F<sub>3</sub> System by Operando High Resolution Synchrotron X-ray Diffraction, *Chem. Mater.* 27 (2015) 3009–3020. <https://doi.org/10.1021/acs.chemmater.5b00361>.

[45] T. Waldmann, G. Bisle, B.-I. Hogg, S. Stumpp, M.A. Danzer, M. Kasper, P. Axmann, M. Wohlfahrt-Mehrens, Influence of Cell Design on Temperatures and Temperature Gradients in Lithium-Ion Cells: An In Operando Study, *J. Electrochem. Soc.* 162 (2015) A921–A927. <https://doi.org/10.1149/2.0561506jes>.

[46] L.H.B. Nguyen, P. Sanz Camacho, T. Broux, J. Olchowka, C. Masquelier, L. Croguennec, D. Carlier, Density Functional Theory-Assisted <sup>31</sup>P and <sup>23</sup>Na Magic-Angle Spinning Nuclear Magnetic Resonance Study of the Na<sub>3</sub>V<sub>2</sub>(PO<sub>4</sub>)<sub>2</sub>F<sub>3</sub>–Na<sub>3</sub>V<sub>2</sub>(PO<sub>4</sub>)<sub>2</sub>FO<sub>2</sub> Solid Solution: Unraveling Its Local and Electronic Structures, *Chem. Mater.* 31 (2019) 9759–9768. <https://doi.org/10.1021/acs.chemmater.9b03546>.

[47] R.J. Colton, A.M. Guzman, J.W. Rabalais, Electrochromism in some thin-film transition-metal oxides characterized by x-ray electron spectroscopy, *J. Appl. Phys.* 49 (1978) 409–416. <https://doi.org/10.1063/1.324349>.

[48] A. Benayad, H. Martinez, A. Gies, B. Pecquenard, A. Levasseur, D. Gonbeau, XPS investigations achieved on the first cycle of V<sub>2</sub>O<sub>5</sub> thin films used in lithium microbatteries, *J. Electron Spectros. Relat. Phenomena.* 150 (2006) 1–10. <https://doi.org/10.1016/j.elspec.2005.09.001>.

[49] S. Verdier, L. El Ouatani, R. Dedryvère, F. Bonhomme, P. Biensan, D. Gonbeau, XPS Study on Al<sub>2</sub>O<sub>3</sub>- and AlPO<sub>4</sub>-Coated LiCoO<sub>2</sub> Cathode Material for High-Capacity Li Ion Batteries, *J. Electrochem. Soc.* 154 (2007) A1088. <https://doi.org/10.1149/1.2789299>.

[50] S. Komaba, W. Murata, T. Ishikawa, N. Yabuuchi, T. Ozeki, T. Nakayama, A. Ogata, K. Gotoh, K. Fujiwara, Electrochemical Na insertion and solid electrolyte interphase for hard-carbon electrodes and application to Na-ion batteries, *Adv. Funct. Mater.* 21 (2011) 3859–3867. <https://doi.org/10.1002/adfm.201100854>.

[51] J.P. Pender, G. Jha, D.H. Youn, J.M. Ziegler, I. Andoni, E.J. Choi, A. Heller, B.S. Dunn, P.S. Weiss, R.M. Penner, C.B. Mullins, Electrode Degradation in Lithium-Ion Batteries, *ACS Nano.* 14 (2020) 1243–1295. <https://doi.org/10.1021/acsnano.9b04365>.

[52] A. Banerjee, Y. Shilina, B. Ziv, J.M. Ziegelbauer, S. Luski, D. Aurbach, I.C. Halalay, Review—Multifunctional Materials for Enhanced Li-Ion Batteries Durability: A Brief Review of Practical Options, *J. Electrochem. Soc.* 164 (2017) A6315–A6323. <https://doi.org/10.1149/2.0451701jes>.

[53] C. Zhan, T. Wu, J. Lu, K. Amine, Dissolution, migration, and deposition of transition metal ions in Li-ion batteries exemplified by Mn-based cathodes-A critical review, *Energy Environ. Sci.* 11 (2018) 243–257. <https://doi.org/10.1039/c7ee03122j>.

[54] R. Mogensen, D. Brandell, R. Younesi, Solubility of the Solid Electrolyte Interphase (SEI) in Sodium Ion Batteries, *ACS Energy Lett.* 1 (2016) 1173–1178. <https://doi.org/10.1021/acseenergylett.6b00491>.